

# A bug on a raft: recoil locomotion in a viscous fluid

STEPHEN CHILDRESS<sup>1</sup>†, SAVERIO E. SPAGNOLIE<sup>1,2</sup>  
AND TADASHI TOKIEDA<sup>3</sup>

<sup>1</sup>Courant Institute of Mathematical Sciences, New York University, 251 Mercer Street,  
New York, NY 10012, USA

<sup>2</sup>Department of Mechanical and Aerospace Engineering, University of California, San Diego,  
9500 Gilman Drive, La Jolla, CA 92093, USA

<sup>3</sup>Trinity Hall, Cambridge CB2 1TJ, UK

(Received 13 March 2010; revised 30 September 2010; accepted 30 September 2010;  
first published online 12 January 2011)

The locomotion of a body through an inviscid incompressible fluid, such that the flow remains irrotational everywhere, is known to depend on inertial forces and on both the shape and the mass distribution of the body. In this paper we consider the influence of fluid viscosity on such inertial modes of locomotion. In particular we consider a free body of variable shape and study the centre-of-mass and centre-of-volume variations caused by a shifting mass distribution. We call this *recoil locomotion*. Numerical solutions of a finite body indicate that the mechanism is ineffective in Stokes flow but that viscosity can significantly increase the swimming speed above the inviscid value once Reynolds numbers are in the intermediate range 50–300. To study the problem analytically, a model which is an analogue of Taylor’s swimming sheet is introduced. The model admits analysis at fixed, arbitrarily large Reynolds number for deformations of sufficiently small amplitude. The analysis confirms the significant increase of swimming velocity above the inviscid value at intermediate Reynolds numbers.

**Key words:** propulsion, swimming/flying

---

## 1. Introduction

In the study of Newton’s concept of momentum, a classic problem concerns the conservation of momentum when mass is redistributed on a floating body. We state this here as a ‘bug on a raft’ problem. A bug of mass  $m$  moves on a small finite raft of mass  $M$ , which floats on an incompressible fluid. The position of the centre of mass of the raft is  $X(t)$ , and the position of the bug is  $X(t) + x(t)$ , assuming movement on a line. If the fluid is inviscid, no fluid forces are applied to the raft, and we shall take its virtual mass to be zero. By conservation of linear momentum, assuming no initial movement of the raft, bug or fluid, we must have vanishing momentum at all times:

$$P(t) \equiv M\dot{X} + m(\dot{X} + \dot{x}) = 0. \quad (1.1)$$

Thus

$$\dot{X} = -\frac{m}{M+m}\dot{x}. \quad (1.2)$$

† Email address for correspondence: childress@cims.nyu.edu

If the bug moves a distance  $L$ , the centre of the raft moves in the opposite direction a distance  $-[m/(m+M)]L$ . Since the centre of mass is  $X(t) + [m/(M+m)]x(t)$ , we see by differentiation and use of (1.2) that it does not change in time. If, on the other hand, we suppose the fluid to be very viscous and assume that the viscous force acting on the raft is  $-\lambda\dot{X}$ , i.e. proportional to the velocity of the raft with constant  $\lambda$ , then according to Newton's second law

$$\frac{dP}{dt} = -\lambda\dot{X}(t) \quad (1.3)$$

so that

$$(M+m)\ddot{X} + m\ddot{x} = -\lambda\dot{X}. \quad (1.4)$$

Suppose now that the bug moves a distance  $L$  in time  $T$  and then remains at rest. After the movement the raft acquires a velocity, which for  $t > T$  decays according to

$$(M+m)\ddot{X} + \lambda\dot{X} = 0. \quad (1.5)$$

This exponential decay ensures that (1.4) is integrable with respect to  $t$  from 0 to  $\infty$ , yielding

$$(M+m)[\dot{X}(\infty) - \dot{X}(0)] + m[\dot{x}(\infty) - \dot{x}(0)] = -\lambda[X(\infty) - X(0)] \quad (1.6)$$

$$\implies \lambda[X(\infty) - X(0)] = 0, \quad (1.7)$$

so the net translation of the raft is zero. Meanwhile the centre of mass has moved a distance  $[m/(M+m)]L$ .

This last conclusion is independent of the value of  $\lambda$ . Yet if  $\lambda$  vanishes, the raft moves! The limit  $\lambda \rightarrow 0$  is therefore singular: the smaller the  $\lambda$ , the longer one has to wait for decay to occur. For example, let the mass  $m$  be accelerated instantaneously to velocity  $L/T$  for a time  $T$  and then brought to rest. For  $t > T$  we have

$$X(t) = -\frac{mL}{\lambda T} \left[ \exp\left(\frac{\lambda T}{m+M}\right) - 1 \right] \exp\left(-\frac{\lambda t}{m+M}\right). \quad (1.8)$$

This example illustrates the peculiar role of viscosity in the dynamics of the bug-raft system, and it is these observations which prompted the present investigation. In this paper we shall examine the role of viscosity on locomotion in a related system involving simultaneous changes of the shape and the distribution of mass of a body. Saffman (1967) has studied the possibility of inertial locomotion of a finite body in an *inviscid* fluid. If the system starts from rest, the fluid flow remains irrotational by Kelvin's theorem, and Saffman showed that the resulting potential flow could involve locomotion of the body by varying in time the body's *virtual mass*. The latter term refers to the 'added' mass associated with the momentum created in the fluid surrounding the body. Although no net momentum is produced in the process, the centre of volume can be changed, and if the deformation is cyclic, these deformations can advance the body by a fixed distance over each cycle. For periodic deformation and motion along a line, for example, the centre of mass of the body will occupy the same position relative to the centre of volume at the end of each cycle. However the centre of mass of the body and the fluid, computed by a suitable limiting process in the case of an infinite domain, will separate from the centre of volume of the body. The resulting movement of the body will be termed *recoil locomotion*.

To see this in the simplest setting, imagine that a time-dependent virtual mass could be associated with our raft, by altering the shape of its bottom for example. (We shall introduce such a model in §3.) With  $M$  a function of time we then have for an

inviscid fluid

$$\dot{X} = -\frac{m}{M(t) + m}\dot{x}. \quad (1.9)$$

If  $x$  leads  $M$  in phase by  $90^\circ$ , this will lead to motion to the right. For example, if  $x = L \sin(\omega t + \theta)$ ,  $M = M_0 + M_V(t)$ ,  $M_V = m_0 \cos \omega t$  with  $0 < m_0 < M_0 + m$ , we have

$$X = -mL\omega \int \frac{\cos(\omega t + \theta) dt}{M_0 + m + m_0 \cos \omega t}. \quad (1.10)$$

The quadrature yields an advance of

$$\Delta X = 2\pi L \frac{m}{m_0} \left[ \frac{M_0 + m}{\sqrt{(M_0 + m)^2 - m_0^2}} - 1 \right] \cos \theta \quad (1.11)$$

per cycle of period  $2\pi/\omega$ . The maximum speed is obtained by aligning the extrema of the velocity of the mass  $m$  and that of  $M(t)$ .

Let us again add a viscous resistance  $-\lambda\dot{X}$  and assume for simplicity that  $\lambda$  is a constant which can be set independent of  $M(t)$ . We then have

$$\frac{d}{dt}([M(t) + m]\dot{X} + m\dot{x}) = -\lambda\dot{X}. \quad (1.12)$$

From this we see that if  $X$  is a solution of (1.12) for some given periodic  $x(t)$  such that  $M$  and  $\dot{X}$  are periodic with the same period as  $x$ , then necessarily  $X(0) = X(T)$  and no locomotion occurs. To prove this it suffices again to integrate both sides of (1.12) from 0 to  $T$  and use the assumed periodicity.

To see the movement in a special case, suppose that the mass moves discontinuously with velocities  $\pm u$  and that the raft mass varies discontinuously between the values  $M_1$  and  $M_2$ . That is, first with  $M = M_1$  the bug accelerates instantaneously to velocity  $+u$  for a time  $T = L/u$ ; then with  $M = M_2$  the bug accelerates instantaneously to velocity  $-u$  for time  $T$ , and so on. Denote by  $U(0+)$  the velocity of the raft after the first acceleration. Then at  $T-$  the velocity of the raft is  $U(T-) = U(0+) \exp[-\lambda T/(m + M_1)]$ , and the total momentum is  $mu + (m + M_1)U(0+) \exp[-\lambda T/(m + M_1)]$ . Thus by conservation of momentum

$$mu + (m + M_1)U(0+) \exp\left(-\frac{\lambda T}{m + M_1}\right) = -mu + (m + M_2)U(T+). \quad (1.13)$$

Solving for  $U(T+)$  and allowing for decay we obtain

$$U(2T-) = \left[ \frac{2mu}{m + M_2} + \frac{m + M_1}{m + M_2} U(0+) \exp\left(-\frac{\lambda T}{m + M_1}\right) \right] \exp\left(-\frac{\lambda T}{m + M_2}\right). \quad (1.14)$$

Again by conservation of momentum,

$$-mu + (m + M_2)U(2T-) = mu + (m + M_1)U(2T+). \quad (1.15)$$

Thus

$$U(2T+) = \frac{2mu}{m + M_1} \left[ \exp\left(-\frac{\lambda T}{m + M_2}\right) - 1 \right] + U(0+) \exp\left[-\lambda T \left( \frac{1}{m + M_1} + \frac{1}{m + M_2} \right)\right]. \quad (1.16)$$

The fixed point  $U(0+) = U(2T+) \equiv U$  is given by

$$U = \frac{2\mu}{m + M_1} \left\{ \frac{\exp\left(-\frac{\lambda T}{m + M_2}\right) - 1}{1 - \exp\left[-\lambda T \left(\frac{1}{m + M_1} + \frac{1}{m + M_2}\right)\right]} \right\}. \quad (1.17)$$

We see from the recursion (1.16) that this fixed point is stable. Moreover the distance covered in time  $T$  with velocity  $U(0+)\exp[-\lambda t/(m + M_1)]$  is equal in length and opposite in sign to that covered with velocity  $U(T+)\exp[-\lambda t/(m + M_2)]$  in time  $T$ . Thus there is no locomotion.

What if the  $\lambda$  values are also changed with the  $M$  values? In general we would expect this to occur. All of our results for velocity look the same, with decay factors replaced by  $\exp[-\lambda_i T/(m + M_i)]$ ,  $i = 1, 2$ . But in the final calculation of the distance travelled in the two half-periods, the distances differ by a factor  $\lambda_1/\lambda_2$ . Thus there is locomotion. Note that the translation in one cycle is  $O(\lambda^{-1})$ , indicating that the speed of recoil locomotion at small Reynolds numbers should be of order  $L^2\omega/\nu$  for a body of size  $L$ .

We could adopt (1.12) with  $\lambda = \lambda(t)$  as a model which combines viscous and virtual-mass effects. However this equation combines the drag law for Stokes flow of a finite body in three dimensions with the virtual momentum of a perfect fluid flow about such a body. In reality the time-dependent viscous drag and the inertial effects do not so easily separate at finite Reynolds number. Nor can we independently prescribe drag and virtual mass. Nevertheless it is clear that by suitable variations of drag in concert with the variation of virtual mass, it could be possible to enhance locomotion in a viscous fluid, despite the implications of viscous dissipation. But the question remains: how do these effects combine in general, and how well does a body move in a viscous fluid, using recoil locomotion?

To explore this problem, we first present in §2 the results of numerical calculations of a finite body in two spatial dimensions. Dimension two is permissible here, despite the implications of the Stokes paradox of steady flow, because of the periodic flow field developed during locomotion. The body is equipped with a moving internal mass and changes shape as a time-dependent ellipse. We shall show that, over an intermediate range of Reynolds numbers, the swimming speed may be increased above the inviscid value by a factor of almost 3. At these Reynolds numbers, any hope of an analysis of the locomotion requires a perturbative approach, and we introduce such a model in §3. Our model, which is again two-dimensional and periodic in space and time, is similar in spirit to the seminal swimming sheet model of G. I. Taylor (1951). The analysis of this model, in §§4 and 5, confirms the possibility of locomotive enhancement by viscous effects by a factor  $\sim 3$  (cf. figure 12). In §6 we compare, with partial success, the results for the infinite model with the simulations of a finite body. Our conclusions regarding the viscous effects in recoil locomotion are summarized in the discussion in §7.

## 2. Recoil locomotion of a finite body in two dimensions

We consider now a system consisting of an elliptic body of periodically varying aspect ratio, containing within it a mass (our ‘bug’) of variable position. We shall study the locomotion of the body by direct numerical simulation. The subscript  $f$  is used to indicate the parameters appropriate to our finite body. Later (in §7) we shall

compare these calculations with results obtained analytically for a fluctuating sheet of infinite extent.

The two-dimensional elliptic boundary of the body has prescribed semi-major and semi-minor axis lengths  $\mathcal{L}_f a(\omega_f t)$  and  $\mathcal{L}_f c(\omega_f t)$  and undergoes periodic, area-preserving shape deformations:  $Area = \pi \mathcal{L}_f^2 a(\omega_f t) c(\omega_f t) = \text{constant}$ . The system is made dimensionless by scaling on the length  $\mathcal{L}_f = \sqrt{Area/\pi}$ , velocity  $\mathcal{U}_f = \mathcal{L}_f \omega_f$  and time  $\mathcal{L}_f/\mathcal{U}_f$ . Then  $R_f = \rho \omega_f \mathcal{L}_f^2/\mu$  is a frequency Reynolds number, with  $\rho$  the fluid density and  $\mu$  the dynamic viscosity. The length scale is chosen so that  $a(\tau)c(\tau) = 1$ .

To compute the fluid–body interaction, the vorticity/stream-function formulation of the Navier–Stokes equations (3.10) is solved implicitly and with high accuracy on a time-dependent body-conforming grid, using a mixed Fourier/finite-difference spatial discretization. The fluid equations are coupled with an equation for the lateral body acceleration. The numerical method is described in detail by Spagnolie & Shelley (2009) and is a variation on a well-studied scheme described by E & Liu (1996) and Alben (2008). The boundary conditions are no-slip on the body surface and decaying fluid velocity in the far field.

Horizontal momentum balance gives (in dimensional variables)

$$M\ddot{X} + m(\ddot{X} + \ddot{x}) = \mathbf{i} \cdot \mathbf{F}(t), \quad (2.1)$$

where  $\mathbf{i} \cdot \mathbf{F}(t)$  is the horizontal fluid force acting on the body surface  $\partial D$ . A convenient representation of the fluid force is achieved through a manipulation of the velocity/pressure form of the Navier–Stokes equations, which can be written as an integration against the vorticity  $-\Delta\psi^*$  and its normal derivative  $\partial_n(-\Delta\psi^*)$  on the body surface, where  $(\psi_y^*, -\psi_x^*)$  is the fluid velocity. Parameterizing the surface by the azimuthal angle  $\phi' \in [0, 2\pi)$ , we have

$$\mathbf{i} \cdot \mathbf{F}(t) = \pi\rho \mathcal{L}_f^2 \ddot{X} + \mu \mathbf{i} \cdot \int_0^{2\pi} (\mathbf{x}^\perp \partial_n(\Delta\psi^*) - \mathbf{x}_\theta \Delta\psi^*)|_{\partial D} d\phi', \quad (2.2)$$

with  $\mathbf{x}^\perp = (-y, x)$ . Upon non-dimensionalization and setting the mass's position relative to the centre of volume as  $x(t) = L \sin(\omega_f t - \theta_f)$ , the body's centre-of-volume acceleration may be written as

$$\chi_{\tau\tau} = \frac{\alpha_f}{(1 - \beta_f)} \sin(\tau - \theta_f) + \frac{\beta_f}{\pi(1 - \beta_f)R_f} \int_0^{2\pi} (\mathbf{x}^\perp \partial_n(\Delta\psi) - \mathbf{x}_\theta \Delta\psi)|_{\partial D} d\phi', \quad (2.3)$$

where

$$\chi = \mathcal{L}_f^{-1} X, \quad \tau = \omega_f t, \quad \alpha_f = \frac{mL}{\mathcal{L}_f(M+m)}, \quad \beta_f = \frac{\pi\rho \mathcal{L}_f^2}{M+m}. \quad (2.4)$$

We have set  $\psi^* = \mathcal{L}_f^2 \omega_f \psi$ , and  $\mathbf{x}$  is now understood to be dimensionless. The parameter  $\alpha_f$  may be viewed as a measure of the momentum of the bug relative to the momentum of the elliptic body and the bug, and the parameter  $\beta_f$  measures the virtual mass of the body relative to the actual mass of the body and the bug. It will be informative to split the fluid force into two parts:

$$\mathbf{i} \cdot \mathbf{F}(t) = \frac{(M+m)\mathcal{U}_f^2}{\mathcal{L}_f} (F_p(t) + F_v(t)), \quad (2.5)$$

a ‘pressure drag’ term  $F_p(t)$  which tends to the virtual mass contribution in the infinite-Reynolds-number limit,

$$F_p(t) = \beta_f \chi_{\tau\tau} + \frac{\beta_f}{\pi R_f} \int_0^{2\pi} \mathbf{x}^\perp \partial_n (\Delta \psi)|_{\partial D} d\phi', \quad (2.6)$$

and a ‘viscous drag’ term  $F_v(t)$ ,

$$F_v(t) = -\frac{\beta_f}{\pi R_f} \int_0^{2\pi} \mathbf{x}_\theta \Delta \psi|_{\partial D} d\phi'. \quad (2.7)$$

In the inviscid theory,  $F_v(t)$  vanishes, and the second term of (2.6) contributes another term proportional to  $\chi_{\tau\tau}$ ; the  $\chi_{\tau\tau}$  terms then combine to yield a virtual mass. For flow past a circular cylinder at Reynolds number equal to 100, experiments and simulations have shown that approximately 80% of the total drag is due to the pressure drag (see Roshko 1961; Braza, Chassaing & Ha Minh 1986).

Assuming a sinusoidally varying virtual mass, the inviscid theory gives

$$\frac{\partial}{\partial t} [(1 + \tilde{\beta}(\tau))\chi_\tau + \alpha_f \cos(\tau - \theta_f)] = 0, \quad (2.8)$$

where

$$\tilde{\beta}(\tau) = \frac{\pi \rho c(\tau)^2 \mathcal{L}_f^2}{M + m} = \tilde{\beta}_0 + \tilde{\beta}_1 \cos(\tau). \quad (2.9)$$

After integrating (assuming zero initial total momentum), the swimming speed  $U_f$  is

$$U_f = \langle \chi_\tau \rangle = \frac{\alpha_f}{\tilde{\beta}_1} \left( \frac{1 + \tilde{\beta}_0}{\sqrt{(1 + \tilde{\beta}_0)^2 - \tilde{\beta}_1^2}} - 1 \right) \cos \theta_f. \quad (2.10)$$

For the case  $\theta_f = 0$ , (2.8) indicates that the centre of volume takes its largest negative and positive velocities at times  $\tau = 2\pi n$  and  $\tau = 2\pi n + \pi$  ( $n = 0, 1, 2, \dots$ ) respectively. The largest velocity variations about the mean in this case are therefore

$$\max_\tau (\chi_\tau - \langle \chi_\tau \rangle) = \frac{\alpha_f}{1 + \tilde{\beta}_0 - \tilde{\beta}_1} - \langle \chi_\tau \rangle = \|\chi_\tau - \langle \chi_\tau \rangle\|_\infty, \quad (2.11)$$

$$\min_\tau (\chi_\tau - \langle \chi_\tau \rangle) = -\frac{\alpha_f}{1 + \tilde{\beta}_0 + \tilde{\beta}_1} - \langle \chi_\tau \rangle. \quad (2.12)$$

The mean and maximal velocities achieved in the inviscid theory grow without bound as  $\tilde{\beta}_1$  approaches  $1 + \tilde{\beta}_0$ . This corresponds to the case in which the body becomes infinitely slender along its major axis during one stage of the recoil forcing, and since there is no viscous drag, there is no resistance whatsoever during this part of the cycle. With the inclusion of viscous dissipation, the question of optimal shape for recoil locomotion remains, since there is in general an unbounded, increasing viscous drag on a flat plate of increasing length. In the limit as  $\tilde{\beta}_1 \rightarrow 1 + \tilde{\beta}_0$  from below, the maximal velocity amplitude grows as

$$\|\chi_\tau - \langle \chi_\tau \rangle\|_\infty \sim \alpha_f (1 + \tilde{\beta}_0 - \tilde{\beta}_1)^{-1}, \quad (2.13)$$

whereas the mean velocity grows at an asymptotically slower rate,

$$U_f = \langle \chi_\tau \rangle \sim \frac{\alpha_f}{\sqrt{2(1 + \tilde{\beta}_0)}} (1 + \tilde{\beta}_0 - \tilde{\beta}_1)^{-1/2}. \quad (2.14)$$

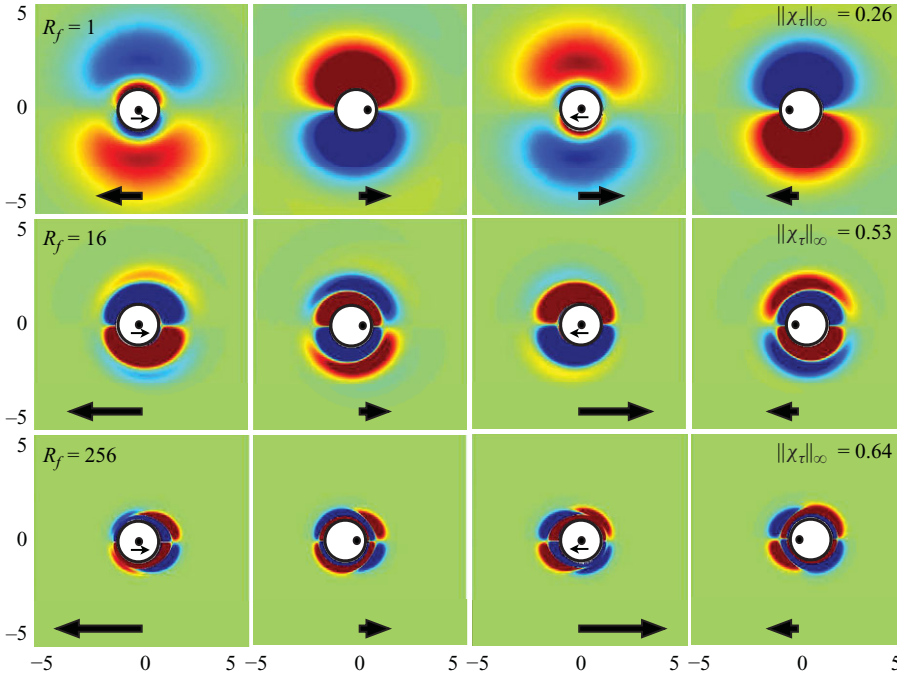


FIGURE 1. The vorticity profiles generated by an oscillating cylinder for three different Reynolds numbers are shown at four equally spaced times during the second period of oscillation, with  $\alpha_f = 1$  and  $\beta_f = 1/2$ . Red corresponds to positive (counterclockwise) vorticity and blue to negative (clockwise) vorticity. The small arrows indicate the velocity of the mass, while the large arrows indicate the velocity of the raft.

### 2.1. Fixed cylindrical body

Before studying the shape-changing body, we first consider the behaviour of a cylinder of fixed shape,  $a(\tau) = c(\tau) = 1$ , and set  $\theta_f = 0$  without loss of generality. In the inviscid theory,  $F_v(t) = 0$  while  $F_p(t) = -\beta \chi_{\tau\tau}$ . Hence, the dynamics is governed by

$$(1 + \beta_f)\chi_{\tau\tau} = \alpha_f \sin \tau, \tag{2.15}$$

and therefore (with  $\chi_\tau(0) = 0$ ),

$$\chi_\tau = -\frac{\alpha_f}{1 + \beta_f}(\cos \tau - 1). \tag{2.16}$$

The body simply oscillates back and forth with zero net motion. In this case there is no time lag between the oscillatory motion of the boundary and the motion of the mass, and they move together in step (in opposite directions).

Figure 1 shows the vorticity profiles generated by the system, using  $\alpha_f = 1$  and  $\beta_f = 1/2$  (the body is massless, and the moving mass is twice that of the displaced fluid). Red corresponds to positive (counterclockwise) vorticity and blue to negative (clockwise) vorticity. The second period of motion is shown at four equally spaced moments in time for a selection of Reynolds numbers. At  $R_f = 1$  the body moves promptly upon the application of the recoil force from within and slows rapidly when the internal forcing is small and changing sign. When the raft is accelerating to the right, as in the second column (from the left) of figure 1 ( $\tau = 1.25$ ), vorticity

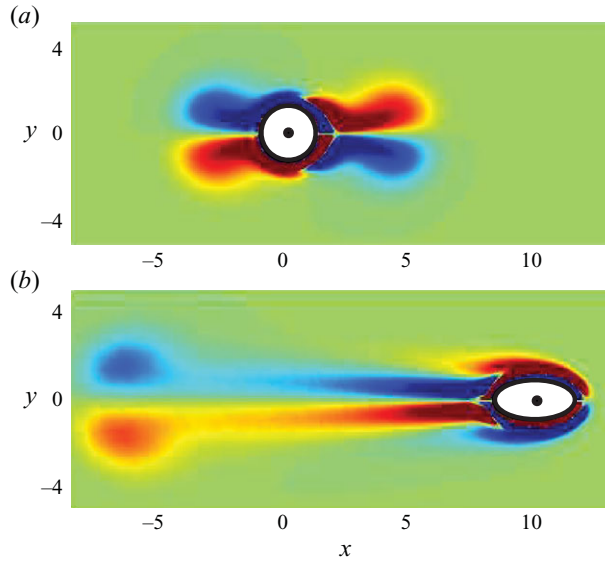


FIGURE 2. Vorticity profiles generated by recoil forcing for (a) a body of fixed shape and (b) a shape-changing body at  $R = 256$  after 20 periods of oscillation.

is developed in the boundary layer which extends well into the surrounding fluid. As the body decelerates, vorticity of opposite sign is generated at the surface; the previously developed vorticity detaches from the raft and decays rapidly because of viscous dissipation.

At a larger Reynolds number  $R_f = 16$ , the vortex dipoles created in the wake of the body on each half-period are more pronounced, and the boundary layer does not extend as far vertically into the fluid. At  $R_f = 256$ , the vortex dipoles created on each half-period are still present when the body returns. The vortex-quadrupole structure is maintained with the addition of vorticity on each passing visit. Unlike in the previous two cases, the system has not yet approached a periodic steady state, and the wake is only just beginning to develop. The vortical structure present after 20 periods of oscillation is shown in figure 2(a).

The flow generated by an oscillating cylinder in a quiescent fluid in two dimensions with prescribed velocity has been investigated by Tatsuno & Bearman (1990) and Elston, Blackburn & Sheridan (2006). At low to intermediate Reynolds numbers the viscous dissipation is sufficient so that there are no persistent up/down asymmetries which form in the wake, just as in the three cases shown here. For larger Reynolds numbers this is not the case (see the references above).

Figure 3(a) shows the maximum velocity reached by the oscillating cylindrical body. As  $R_f \rightarrow 0$  the motion ceases entirely, as indicated by (2.3): the exact solution at  $R_f = 0$  (assuming  $\beta_f = O(1)$ ) is simply a quiescent system,  $\psi = \chi_\tau = 0$ . However, recoil swimming is still possible at zero Reynolds number as long as the internal mass is very large,  $\beta_f = O(R_f)$  as  $R_f \rightarrow 0$ . Meanwhile, as  $R_f \rightarrow \infty$ , the maximum body velocity tends to the inviscid theory result with apparent scaling  $\|\chi_\tau\|_\infty \sim R_f^{-1}$ , as shown in the inset of figure 3(a).

Figure 3(b) shows a lead-time  $\tilde{\phi}_f$  as a function of the Reynolds number. For sinusoidal motion, the lead-time is defined implicitly by  $\chi_\tau = -\cos(\tau + \tilde{\phi}_f)$ . Generally, we compute the lead-time by subtracting the times corresponding to the body's and

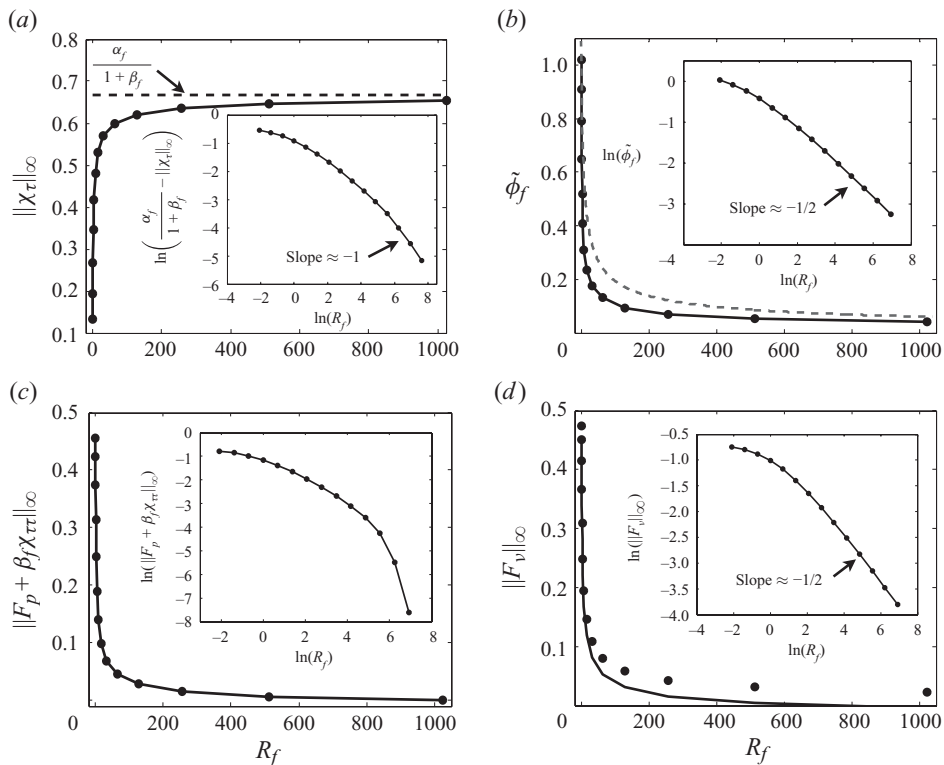


FIGURE 3. Data for the body of fixed shape (an oscillating cylinder), as functions of the Reynolds number  $R_f$ . (a) Maximal centre-of-volume velocity, and departure from the inviscid theory limit on a logarithmic scale (inset). (b) Lead-time, and on a logarithmic scale (inset). Approximate values using  $C=1$  are shown as the dashed line (see (2.19)). (c) Maximal departure of the pressure drag from the inviscid theory limit, and the same on a logarithmic scale (inset). (d) Maximal viscous drag, and on a logarithmic scale (inset).

the internal mass's zero velocity. When the internal mass is accelerating to the right, it imparts a recoil force on the body to the left. However, when the mass has almost reached its peak velocity, the recoil force is still to the left, but the fluid drag can become dominant, setting the body into its own deceleration in advance of the mass's inflection point. Hence, we expect that the lead-time  $\tilde{\phi}_f$  tends to zero as  $R_f \rightarrow \infty$ , and since the body motion begins and ceases instantly upon the application or withdrawal of force at  $R_f=0$ , we expect that  $\tilde{\phi}_f \rightarrow \pi/2$  as  $R_f \rightarrow 0$ . Figure 3(b) confirms these expectations, and we find a decay to zero as  $R_f \rightarrow \infty$  that scales as  $\tilde{\phi}_f \sim R_f^{-1/2}$ .

Figures 3(c) and 3(d) show the departures of the pressure and viscous drags from their inviscid theory limits. As  $R_f \rightarrow \infty$  the viscous drag decays to zero as  $F_v \sim R_f^{-1/2}$ , along with the size of the viscous boundary layer. Meanwhile, the departure of the pressure drag from the inviscid limit ( $F_p(t) = -\beta_f \chi_{\tau\tau}$ ) is dramatic with decreasing  $R_f$  in the low- to intermediate-Reynolds-number regime.

The simulations indicate that  $F_p(t) = -\beta_f \chi_{\tau\tau} + o(R_f^{-1/2})$  and  $F_v = -C R_f^{-1/2} \chi_{\tau} + o(R_f^{-1/2})$  for a constant  $C \approx 1$ . Inserting these expressions into (2.3) we have

$$(1 + \beta_f) \chi_{\tau\tau} = \alpha_f \sin(\tau) - \frac{C}{\sqrt{R_f}} \chi_{\tau} + O\left(\frac{1}{R_f}\right), \quad (2.17)$$

which gives

$$\chi_\tau = -\frac{\alpha_f}{(1 + \beta_f)^2 + \frac{C^2}{R_f}} \cos(\tau + \tilde{\phi}_f) + O\left(\frac{1}{R_f}\right), \quad (2.18)$$

where

$$\tilde{\phi}_f = \tan^{-1}\left(\frac{C}{(1 + \beta_f)\sqrt{R_f}}\right). \quad (2.19)$$

The lead-time  $\tilde{\phi}_f$  therefore decays to zero like  $\tilde{\phi}_f \sim O(C R_f^{-1/2}/(1 + \beta_f))$  as  $R_f \rightarrow \infty$ , and the numerical results are consistent with this consideration. The lead-times using  $C = 1$  in (2.19) are shown as the dashed line in figure 3(b).

## 2.2. Shape-changing body

Having noted certain behaviours in the above case of the body of fixed shape, we now proceed to reconsider recoil locomotion of a shape-changing body. The shape-changing elliptic body now takes on prescribed axis lengths

$$a(\tau) = \sqrt{\frac{2}{\left(1 + \frac{1}{2}\right) + \left(1 - \frac{1}{2}\right) \cos(\tau)}}, \quad c(\tau) = \frac{1}{a(\tau)}, \quad (2.20)$$

which are chosen so that the aspect ratio varies from  $a(\tau)/c(\tau) = 1$  to  $a(\tau)/c(\tau) = 1/2$  along a path such that the virtual mass in the inviscid theory ( $\propto c(\tau)^2$ ) varies sinusoidally. The form above corresponds to (2.9) with  $\tilde{\beta}_0 = 3/4$  and  $\tilde{\beta}_1 = 1/4$ , and as in the previous consideration we choose  $\alpha_f = 1$  and  $\beta_f = 1/2$ . Hence, the inviscid theory (2.10) predicts a mean velocity of  $U_f = \langle \chi_\tau \rangle \approx 0.0415$  with variations about the mean of  $\max_\tau(\chi_\tau - \langle \chi_\tau \rangle) \approx 0.625$  and  $\min_\tau(\chi_\tau - \langle \chi_\tau \rangle) \approx -0.541$ .

Figure 4 shows the vorticity profiles for the same Reynolds numbers considered in figure 1. At  $R_f = 1$  a vortex quadrupole is generated as the body changes shape. The left–right asymmetry in the fluid wake becomes increasingly visible at  $R_f = 16$  and  $R_f = 256$ . At  $R_f = 16$  the boundary layer detaches at  $\tau = 1$  (left-most column) but stays pinned to the surface when the body is more streamlined at  $\tau = 1.5$  (third column from left). The corresponding decrease in fluid drag yields a larger velocity to the right than to the left on each half-period, and the body swims towards right on average.

At  $R_f = 256$  there is a much stronger interaction with previously shed vortices, as in the case of the corresponding fixed cylinder. However, unlike in the case of the fixed cylinder, a leftward-moving fluid jet opposite the direction of net motion now develops, owing to the time variation of the body's presented surface area. At  $\tau = 1$  (first column) the leftward-moving body generates a vortex dipole on the right as the boundary layer detaches and drifts into the wake. Unlike at lower Reynolds numbers, however, the vorticity does not quickly dissipate. Instead, as the recoil forcing drives the body back towards right, and as the body becomes more streamlined, the previously shed vorticity persists and advects to the left-hand side of the body, where its orientation now corresponds to thrust. In the second half of the oscillation period the body presents a larger surface area to the fluid and inhibits the passage of vorticity to the right-hand side of the body. The conversion of vortex dipoles from drag-type into thrust-type by means of surface area variation was also explored by Spagnolie &

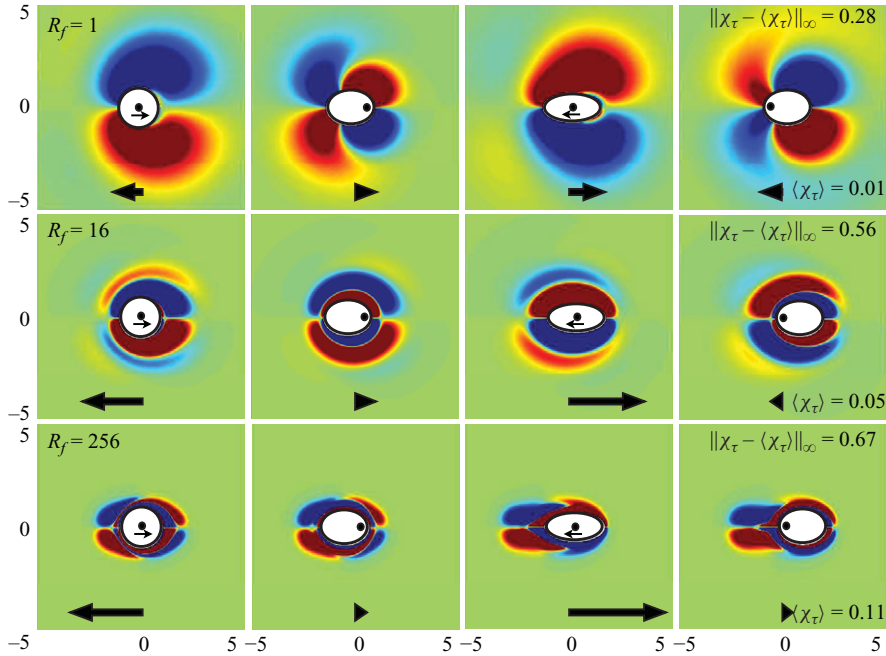


FIGURE 4. The vorticity profiles generated by recoil locomotion at finite Reynolds number are shown at four equally spaced times during the second period of oscillation, again with  $\alpha_f = 1$  and  $\beta_f = 1/2$  as in figure 1. The small arrows indicate the velocity of the mass, while the large arrows indicate the velocity of the body (see also the supplementary movies 1 and 2, which show the dynamics of a shape changing body at  $R = 16$  and  $R = 256$  respectively, available at [journals.cambridge.org/flm](http://journals.cambridge.org/flm)).

Shelley (2009), as generated by a shape-changing body in an oscillatory background flow. The vortical wake after 20 periods is shown in figure 2(b). Movies of the recoil motion of the present study at  $R = 16$  (movie 1) and  $R = 256$  (movie 2) are available online as supplementary material at [journals.cambridge.org/flm](http://journals.cambridge.org/flm).

Figure 5(a) shows the mean velocity attained in the periodic steady state of the shape-changing body. The values are taken once the velocity returns to within 0.1 % of its value on the previous period. The number of periods required to reach this state increases with the Reynolds number; at  $R_f = 1$  merely 3 periods are required, whereas 17 periods are required at  $R_f = 256$ . The small dashed line in figure 5(a) indicates the mean velocity predicted by the inviscid theory,  $\langle \chi_\tau \rangle = 0.0415$ . The computed mean velocity is increasing towards a value approximately 3 times larger than the inviscid prediction. The inset of figure 5(a) shows the mean velocity normalized by  $\sqrt{R_f}$ , in order to facilitate comparison with  $F(R, \beta)$  in figure 9(a) later in the paper. We observe a local maximum in this normalized mean velocity. The exploration of yet higher Reynolds numbers is prohibitive so far. As  $R_f \rightarrow 0$ , however, it appears that the mean velocity is tending to zero as  $\chi_\tau \sim R_f$ , as we have suggested previously. The departure of the velocity from the mean is shown in figure 5(b). These departures are also tending to values larger than those predicted by the inviscid theory, though not as dramatically as the increase in the mean velocity over the predicted value.

The velocity profiles are shown as functions of time in figure 5(c) for the simulations displayed in figure 4. In addition to the growing amplitude, we observe a phase shift as the Reynolds number is increased. We define again a lead-time  $\tilde{\phi}_f$  by writing

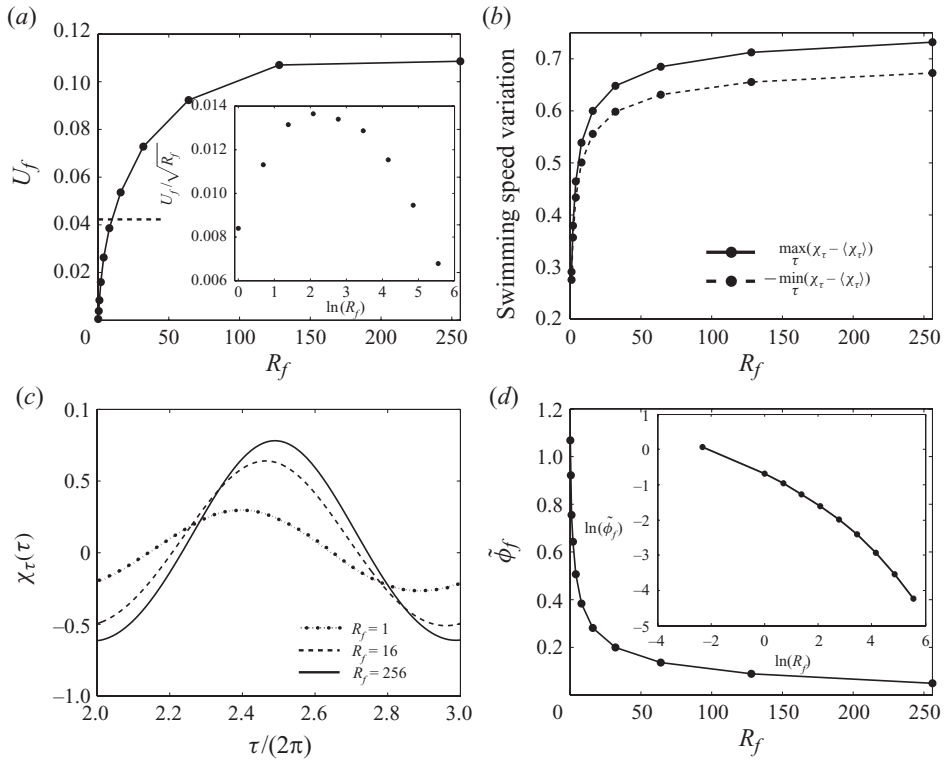


FIGURE 5. Centre-of-volume velocity from simulations of a finite body. (a) The mean velocity, and the same normalized by  $\sqrt{R_f}$  (inset). The small dashed line indicates the mean velocity predicted by the inviscid theory. (b) Velocity amplitudes about the mean. (c) Velocity profiles for the same simulations as shown in figure 4. (d) The lead-time behaves similarly to that in the oscillating cylinder case, though decays here to zero at a faster rate as  $R_f \rightarrow \infty$ .

$\chi_\tau \approx -\cos(\tau + \tilde{\phi}_f)$ . In practice, the first Fourier mode of the numerical data is used to determine the phase shift. The lead-time behaves similarly as the oscillating cylinder case, apparently tending to  $\tilde{\phi}_f = \pi/2$  as  $R_f \rightarrow 0$  and to  $\tilde{\phi}_f = 0$  as  $R_f \rightarrow \infty$ . However, whereas the lead-time has settled to a clear decay in the oscillating cylinder case with scaling  $\tilde{\phi}_f \sim R_f^{-1/2}$  for  $R_f \gg 1$  (see figure 3b), for the same range of Reynolds numbers in the present case the rate of decay is not yet clear and may be decaying faster than  $R_f^{-1/2}$ . This is plausible, since the presented surface area is in this case decreased for part of the cycle, and the inertial component from the virtual mass is smaller on average than in the case of the fixed cylinder.

Plots of the normalized mean velocity as a function of the phase relation  $\theta_f$  between the body's aspect ratio and the mass's position are shown for three Reynolds numbers in figure 6(a). We observe that when the shape change and the mass motion are in phase ( $\theta_f = 0$ ), the body generally does not reach its maximally achievable swimming speed. However, at approximately  $R_f = 30$  this in-phase motion does yield the peak mean swimming velocity. A phase shift  $\Theta_f(R_f)$  is defined here by writing

$$\langle \chi_\tau(\tau; \theta_f, R_f) \rangle \approx \|\chi_\tau(\tau; \theta_f, R_f)\|_\infty \cos(\theta_f + \Theta_f(R_f)), \quad (2.21)$$

where the average is over  $\tau$  and the maximum norm is over  $\theta_f$ . Once again, the first Fourier mode of the numerical data is used to determine the phase shift  $\Theta_f(R_f)$ , which is shown in figure 6(b). There is a clear monotonic trend towards a larger phase shift  $\Theta_f$  as the Reynolds number is increased. Intuition dictates that  $\Theta_f(R_f)$

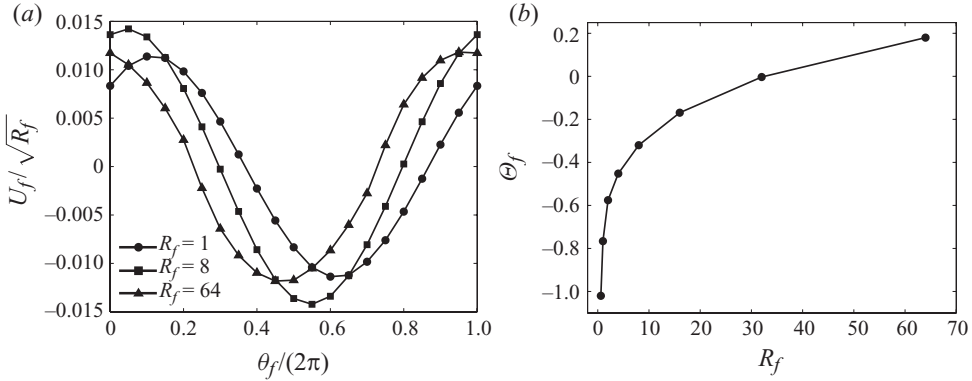


FIGURE 6. (a) Normalized mean velocity as a function of  $\theta_f$ , the phase relation between the body's varying aspect ratio and the mass's position. (b) The phase shift  $\Theta_f(R_f)$ , as defined in the text.

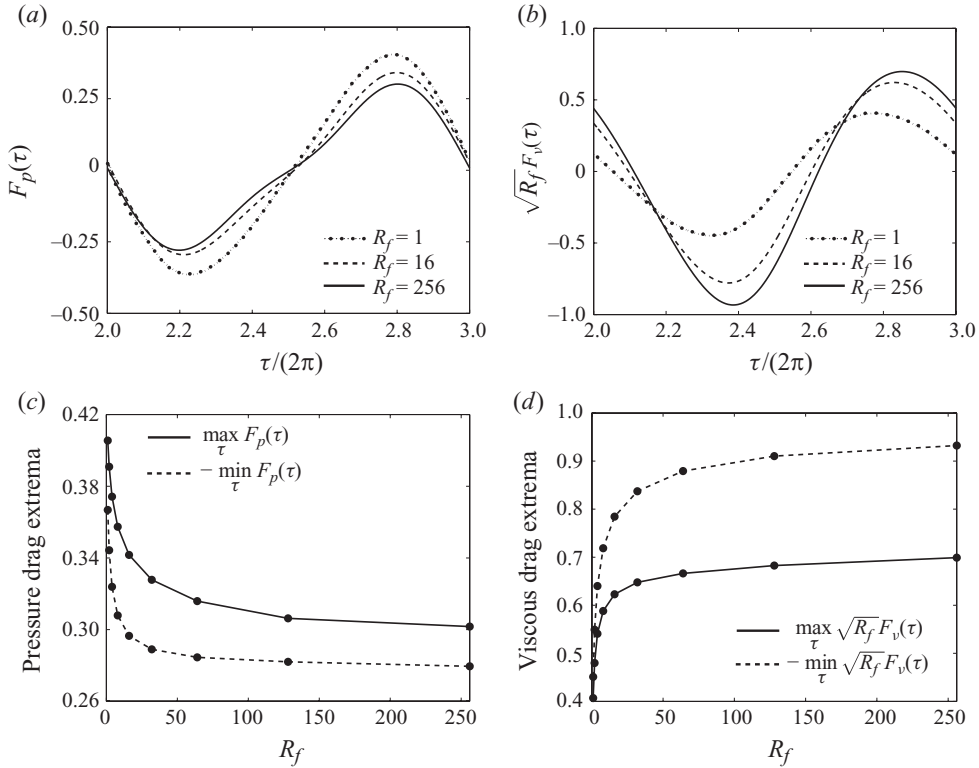


FIGURE 7. (a) Pressure drag through one cycle for the finite shape-changing body at three different Reynolds numbers. (b) Normalized viscous drag through one cycle. (c) Extrema of the pressure drag curves in (a). (d) Extrema of the normalized viscous drag curves in (b).

must tend to a constant in the limit  $R_f \rightarrow \infty$ , but this limit is not yet clear given the Reynolds numbers considered here. The relationship between the lead-time  $\tilde{\phi}_f$  and the phase shift  $\Theta_f$  is discussed in a later section in which the finite body and the infinite raft are compared.

Finally, figures 7(a)–7(d) show the pressure and viscous drags as functions of time, as well as plots of their maxima and minima over a periodic cycle. We observe that the amplitude of the pressure drag tends to a constant value with an error  $O(R_f^{-1/2})$  as

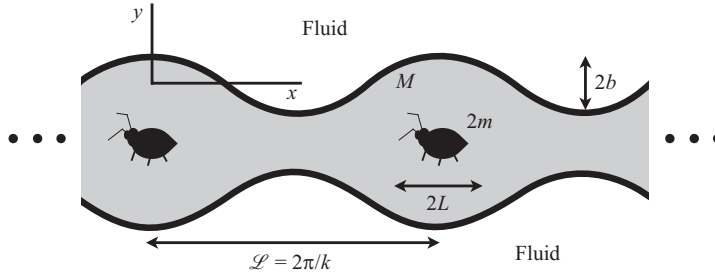


FIGURE 8. Bugs on a deformable raft, symmetrized and periodic in  $x$ .

$R_f \rightarrow \infty$ , while the viscous drag once again decays to zero as  $F_v \sim O(R_f^{-1/2})$ . The gap between the maximum and minimum pressure drag magnitudes, due to the difference in the presented surface area in the elongated and circular shapes, allows for a net recoil locomotion.

### 3. An infinite-sheet model: the deformable raft

In order to formulate a model system which can be analysed mathematically at finite and large Reynolds numbers, we consider a variant of the swimming sheet of G. I. Taylor (1951). If we imagine a periodic array of deforming elliptical bodies in two dimensions, with centres on the  $x$ -axis, their effect on the fluid above or below is similar to that of two wavy sheets undergoing a standing wave, as depicted in figure 8. The oscillating masses are similarly arrayed along the  $x$ -axis. Each sheet may be thought of as an infinite extension of a raft with an oscillating wavy bottom periodic in time.

We choose the spatial period to be  $2\pi/k \equiv \mathcal{L}$ , where  $k$  is the wavenumber. The problem is again completely two-dimensional. We may restrict our attention to the upper domain, where the equation of the raft ‘bottom’ is assumed to be given by

$$x_B(x, t) = X(t), \quad y_B = Y(x, t) = b \sin(\omega t) \sin k(x - X). \quad (3.1)$$

Here, we are in a frame fixed with respect to the fluid at infinity so that the points of the surface of the raft are displaced horizontally by  $X(t)$ . It is important that  $bk$  is assumed small. We will be dealing with a system periodic in time with period  $T = 2\pi/\omega$ . Thus it will be sufficient to consider the system for time  $T$ , where the displacement  $X$  will remain small. Of course to establish a periodic solution may require a long transient time.

The bugs will have mass  $2m$ , per unit length in the ignorable direction, the factor 2 introduced so that a mass  $m$  is associated with each half of the system. The position  $x(t)$  of the  $n$ th bug is given by  $x(t) - x_n - X(t) = L \sin 2(\omega t - \theta)$ , where  $x_n = 2\pi n/k$ ,  $n = 0, \pm 1, \pm 2, \dots$ . The excursion of the mass from left to right is now  $2L$ , and we assume that  $2L < \mathcal{L}$  (see figure 8). The period of the mass movement is half the period of a point on the surface, since the sinusoidal shape means that modulo translation the geometry has period  $\pi/\omega$ . The phase angle  $\theta$  is arbitrary. For the upper half of the system the raft mass per unit length in the  $x$ -direction is assumed to be  $M/\mathcal{L} = M_0/\mathcal{L} + M_V(t)/\mathcal{L}$ , where  $M_0$  is physical mass and  $M_V(t)$  is the virtual mass of one spatial period of the raft. From the symmetry of the system the only movement of the raft is in the  $x$ -direction.

3.1. Recoil locomotion of the raft in an inviscid fluid

This special case is of interest for setting the orders of magnitude of our parameters. The virtual mass  $M_V$ , for a given instantaneous configuration of the raft boundary, may be computed from the kinetic energy in the upper fluid, per spatial period, given that the boundary moves with constant speed  $U$  relative to the fluid at infinity. Since the slope of the raft boundary remains small, the potential in  $y > Y$  may be computed by solving

$$\nabla^2\phi = 0, \quad y > 0, \quad \phi_y|_{y=0} = U \, dY/dx = Ukb \sin(\omega t) \cos kx. \quad (3.2)$$

The solution is

$$\phi = -Ub \sin(\omega t) e^{-ky} \cos kx, \quad (3.3)$$

and the kinetic energy in one spatial period in the upper fluid region is

$$E = \frac{1}{2}\pi\rho U^2 b^2 \sin^2(\omega t). \quad (3.4)$$

Then

$$M = M_0 + M_V(t) = M_0 + \pi\rho b^2 \sin^2(\omega t) \quad (3.5)$$

so that

$$\dot{X} = -\frac{m\dot{x}}{M+m} = -\frac{2\omega m L \cos 2(\omega t - \theta)}{M_0 + m + \frac{1}{2}\pi\rho b^2(1 - \cos 2\omega t)}. \quad (3.6)$$

In preparation for considering the viscous problem and hence the no-slip condition on the raft boundary, we want to make  $\dot{X}$  of the order of the vertical velocity  $\sim b\omega$ . Thus we take  $M_0 \sim m \sim \rho/k^2$ ,  $L \sim b$ . This gives recoil swimming with advance of order  $b^3$  over one temporal period of the motion of the bug and raft boundary. We define the dimensionless variables

$$\epsilon = kb, \quad \tau = \omega t, \quad \chi = kX, \quad \alpha = \frac{Lm}{b(M_0 + m)}, \quad \beta = \frac{\pi\rho}{k^2(M_0 + m)}. \quad (3.7)$$

As in the finite-body calculation, the parameter  $\alpha$  may be viewed as a measure of the momentum of the bug relative to the momentum of the raft and the bug, and the parameter  $\beta$  measures the virtual mass of the raft relative to the actual mass of the raft and the bug. We obtain

$$\chi_\tau = -\frac{2\alpha\epsilon \cos 2(\tau - \theta)}{1 + \frac{1}{2}\beta\epsilon^2(1 - \cos 2\tau)}. \quad (3.8)$$

Then

$$\langle \chi_\tau \rangle = \frac{2\alpha(-2 - \beta\epsilon^2 + 2\sqrt{1 + \beta\epsilon^2}) \cos 2\theta}{\beta\epsilon\sqrt{1 + \beta\epsilon^2}} \sim -\frac{1}{2}\alpha\beta\epsilon^3 \cos 2\theta, \quad (3.9)$$

giving a locomotion speed of order  $\epsilon^3$ .

3.2. Formulation of the viscous problem

We now consider the viscous problem in the upper fluid region, using the stream-function formulation of the two-dimensional Navier–Stokes equations:

$$\frac{\partial \nabla^2 \psi^*}{\partial t} + \psi_y^* \frac{\partial \nabla^2 \psi^*}{\partial x} - \psi_x^* \frac{\partial \nabla^2 \psi^*}{\partial y} - \frac{\mu}{\rho} \nabla^4 \psi^* = 0, \quad (3.10)$$

once again with  $(\psi_y^*, -\psi_x^*)$  the fluid velocity. We will look for a raft motion which is periodic in time. Thus we may consider just one temporal period and try to calculate

the drift of the raft over this period. Our coordinate system assumes the fluid to be at rest at infinity.

To formulate the problem in dimensionless variables, we set  $\xi = kx$ ,  $\eta = ky$ ,  $\tau = \omega t$  and  $\psi^*(x, y, t) = \omega k^{-2} \psi(\xi, \eta, \tau)$ . If  $\Delta \psi = \psi_{\xi\xi} + \psi_{\eta\eta}$ , then (3.10) takes the dimensionless form

$$\frac{\partial \Delta \psi}{\partial \tau} + \psi_{\eta} \frac{\partial \Delta \psi}{\partial \xi} - \psi_{\xi} \frac{\partial \Delta \psi}{\partial \eta} - R^{-1} \Delta^2 \psi = 0, \tag{3.11}$$

where

$$R = \frac{\rho \omega}{k^2 \mu} \tag{3.12}$$

is a frequency Reynolds number. The boundary conditions to be satisfied are, with  $X(t) = k^{-1} \chi(\tau)$  and  $\epsilon = kb$ ,

$$\psi_y^* = dx_B/dt, \quad \text{or } \psi_{\eta} = \chi_{\tau}, \tag{3.13}$$

and

$$\psi_x^* = -dy_B/dt, \quad \text{or } \psi_{\xi} = \epsilon [-\cos \tau \sin(\xi - \chi) + \sin \tau \chi_{\tau} \cos(\xi - \chi)], \tag{3.14}$$

when  $\eta = kY(x, t) \equiv \mathcal{Y}(\xi, \tau) = \epsilon \sin \tau \sin(\xi - \chi)$ . We also require that  $\psi$  vanishes at  $\eta = \infty$ .

We observe that (3.13) and (3.14) imply

$$\frac{\partial}{\partial \xi} \psi(\xi, \mathcal{Y}(\xi, \tau), \tau) = \epsilon [-\cos \tau \sin(\xi - \chi) + 2 \chi_{\tau} \sin \tau \cos(\xi - \chi)]. \tag{3.15}$$

Thus

$$\psi(\xi, \mathcal{Y}(\xi, \tau), \tau) = \epsilon [\cos \tau \cos(\xi - \chi) + 2 \chi_{\tau} \sin \tau \sin(\xi - \chi)] + F(\tau) \tag{3.16}$$

for some  $F(\tau)$ .

### 3.3. Dynamical balance

In dimensional notation the constancy of the total  $x$ -momentum (raft and fluid) is expressed by

$$(m + M_0) \dot{X} + m \dot{x} + \int_0^{2\pi/k} \int_{Y(x,t)}^{\infty} \rho u \, dy \, dx = C^*, \tag{3.17}$$

where we assume that the solution periodic in time has been reached. If we start from a state of rest the constant  $C^*$  will be zero, but this assumes that the integration over space is performed *before* passing to the limit of a periodic solution. The difficulty can be seen most easily in a different problem, where the internal masses accelerate instantaneously to a constant velocity and remain at this velocity. The raft must correspondingly move with a velocity of opposite sign, constant if  $\epsilon = 0$ . Owing to viscous stress, the raft will however slow down, and in the limit of infinite time the equilibrium solution will be reached, with the raft at rest. Still, the total momentum is conserved in this limit: momentum diffuses to infinity, and the fluid velocity tends to zero at any finite point in the limit, but the integrated momentum is fixed.

We shall take the limit first, to achieve a periodic solution before calculating the momentum. Thus

$$(m + M_0) \dot{X} + m \dot{x} = \rho \int_0^{2\pi/k} \psi^*(x, Y(x, t), t) \, dx + C^*, \tag{3.18}$$

where  $C^*$  is unknown but  $\psi$  vanishes at infinity. In dimensionless form

$$\chi_\tau + 2\epsilon\alpha \cos 2(\tau - \theta) = \frac{\beta}{\pi} \int_0^{2\pi} \psi(\xi, \mathcal{Y}, \tau) d\xi + C. \tag{3.19}$$

We shall see presently how the leading non-vanishing term of the mean velocity  $\langle \chi_\tau \rangle$  may be calculated.

### 3.4. The special case $b=0$

The special case  $b=0$  corresponds to the trivial case of a flat-bottomed raft which abuts an infinite expanse of viscous fluid, so the fluid dynamics reduces to a Rayleigh problem generated by a moving mass. Using dimensionless variables,

$$\psi_{\tau\eta} - R^{-1}\psi_{\eta\eta\eta}, \quad \eta > 0, \quad \psi_\eta(\infty, \tau) = 0, \quad \psi_\eta(0, \tau) = \chi_\tau(\tau). \tag{3.20}$$

Any part of  $\psi$  independent of time must vanish by the boundary conditions at infinity, so we have the dynamical balance

$$\chi_\tau + 2\epsilon\alpha \cos(2(\tau - \theta)) = 2\beta\psi(0, \tau). \tag{3.21}$$

Note that  $b$  cancels out of  $\epsilon\alpha$ . Clearly  $\langle \chi_\tau \rangle = 0$ . From the Fourier series for  $\chi$  and the solution of (3.20) we see that  $\chi$  must have the form  $\chi(\tau) = \text{Re}(A \epsilon e^{2i\tau})$  for some complex constant  $A$ . Therefore we must have  $\psi(\eta, \tau) = \text{Re}(P(\eta) e^{2i\tau})$ , where

$$P = -\frac{2iA\epsilon}{\sqrt{2iR}} e^{-\sqrt{2iR}\eta}. \tag{3.22}$$

Then (3.21) implies

$$2iA + 2\alpha e^{-2i\theta} = -\frac{4i\beta}{\sqrt{2iRA}}, \tag{3.23}$$

and therefore

$$A = \frac{i\alpha e^{-2i\theta}}{1 + \frac{2\beta}{\sqrt{2iR}}} = \frac{i\alpha e^{-2i\theta}}{1 + \frac{\beta(1-i)}{\sqrt{R}}}. \tag{3.24}$$

For fixed  $R, \alpha$  and  $\beta$ , all assumed to be of order unity, we thus obtain an oscillation of the raft of order  $\epsilon\alpha$ . We shall retain this ordering when treating the corrugated raft  $b > 0$ .

## 4. Expansion in $\epsilon$ for fixed $R$

The calculations of the present section elaborate the methods used by Tuck (1968) in his analysis of the swimming sheet at finite Reynolds number. We introduce the following expansions in  $\epsilon$  for fixed  $R$ :

$$\chi(\tau) = \epsilon \chi_1(\tau) + \epsilon^2 \chi_2(\tau) + \dots, \quad \psi = \epsilon \psi_1(\xi, \eta, \tau) + \epsilon^2 \psi_2(\xi, \eta, \tau) + \epsilon^3 \psi_3(\xi, \eta, \tau) + \dots \tag{4.1}$$

Also

$$\mathcal{Y} = \epsilon \sin \tau \sin(\xi - \chi) = \epsilon \mathcal{Y}_1 + \epsilon^2 \mathcal{Y}_2 + \dots, \tag{4.2}$$

where

$$\mathcal{Y}_1 = \sin \tau \sin \xi, \quad \mathcal{Y}_2 = -\chi_1 \sin \tau \cos \xi. \tag{4.3}$$

## 4.1. First-order terms

The equation to be satisfied by  $\psi_1$  is

$$\frac{\partial \Delta \psi_1}{\partial \tau} - R^{-1} \Delta^2 \psi_1 = 0, \quad \eta > 0, \quad (4.4)$$

with boundary conditions on  $\eta = 0$ :

$$-\frac{\partial \psi_1}{\partial \xi}(\xi, 0, \tau) = \cos \tau \sin \xi, \quad \frac{\partial \psi_1}{\partial \eta}(\xi, 0, \tau) = \frac{d\chi_1(\tau)}{d\tau}. \quad (4.5)$$

We write

$$\psi_1 = \psi_{10}(\eta, \tau) + \cos \xi \psi_{11}(\eta, \tau), \quad (4.6)$$

where

$$\psi_{11}(0, \tau) = \cos \tau, \quad \frac{\partial \psi_{11}}{\partial \eta}(0, \tau) = 0, \quad (4.7)$$

$$\frac{\partial \psi_{10}}{\partial \eta}(0, \tau) = \frac{d\chi_1(\tau)}{d\tau}. \quad (4.8)$$

The problem for the term  $\psi_{10}$  is identical to the  $b = 0$  case treated above, so we have

$$\psi_{10} = \text{Re}(-A\sqrt{2i/R} e^{-\sqrt{2iR}\eta} e^{2i\tau}), \quad \chi_1(\tau) = \text{Re}(A e^{2i\tau}). \quad (4.9)$$

The solution of the problem for  $\psi_{11}$  is straightforward, and we find

$$\psi_{11} = \text{Re} \left[ \frac{K e^{i\tau}}{K-1} e^{-\eta} + \frac{e^{i\tau}}{1-K} e^{-K\eta} \right], \quad (4.10)$$

where  $K = \sqrt{1+iR}$ .

This completely determines the leading terms of the expansions. No locomotion occurs at this order.

## 4.2. Second-order terms

The equation satisfied by  $\psi_2$  is

$$\frac{\partial \Delta \psi_2}{\partial \tau} - R^{-1} \Delta^2 \psi_2 = -\frac{\partial \psi_1}{\partial \eta} \frac{\partial \Delta \psi_1}{\partial \xi} + \frac{\partial \psi_1}{\partial \xi} \frac{\partial \Delta \psi_1}{\partial \eta}, \quad \eta > 0. \quad (4.11)$$

The conditions at the boundary are

$$[\psi_{1\eta\eta} \mathcal{Y}_1 + \psi_{2\eta}]_{\eta=0} = \dot{\chi}_2, \quad (4.12)$$

$$[\psi_{1\xi\eta} \mathcal{Y}_1 + \psi_{2\xi}]_{\eta=0} = \chi_1 \cos \tau \cos \xi + \chi_{1\tau} \sin \tau \cos \xi. \quad (4.13)$$

We note that  $\psi_{1\xi\eta}(\xi, 0, \tau) = 0$  so that we have

$$\psi_2 = \psi_{20}(\eta, t) + \sin \xi \psi_{21}(\eta, t) + \sin(2\xi) \psi_{22}(\eta, t). \quad (4.14)$$

We now use these equations to prove that the time average  $\langle \dot{\chi}_2 \rangle$  must vanish so that locomotion does not occur at second order either. Let  $\langle \langle \cdot \rangle \rangle$  denote the double average with respect to  $\tau$  and  $\xi$ . Applying this average to (4.11) and using (4.6), we obtain  $d^4 \langle \langle \psi_2 \rangle \rangle / d\eta^4 = 0$ . Thus in particular, given that  $\psi$  must decay as  $\eta \rightarrow \infty$ ,  $\langle \langle \psi_{2\eta} \rangle \rangle|_{\eta=0}$  must vanish. The other term in (4.12) has a vanishing  $\xi$  average, proving the claim.

4.3. Third-order terms

At third order the equations are

$$\begin{aligned} \frac{\partial \Delta \psi_3}{\partial \tau} - R^{-1} \Delta^2 \psi_3 = & -\frac{\partial \psi_2}{\partial \eta} \frac{\partial \Delta \psi_1}{\partial \xi} + \frac{\partial \psi_2}{\partial \xi} \frac{\partial \Delta \psi_1}{\partial \eta}, \\ & -\frac{\partial \psi_1}{\partial \eta} \frac{\partial \Delta \psi_2}{\partial \xi} + \frac{\partial \psi_1}{\partial \xi} \frac{\partial \Delta \psi_2}{\partial \eta}, \quad \eta > 0. \end{aligned} \quad (4.15)$$

The boundary conditions are

$$\begin{aligned} \left. \frac{\partial \psi_3}{\partial \eta} \right|_{\eta=0} = & \left[ -\frac{\partial^2 \psi_2}{\partial \eta^2} \mathcal{Y}_1 - \frac{\partial^2 \psi_1}{\partial \eta^2} \mathcal{Y}_2 - \frac{\partial^3 \psi_1}{\partial \eta^3} \mathcal{Y}_1^2 / 2 \right]_{\eta=0} + \dot{\chi}_3, \quad (4.16) \\ \left. \frac{\partial \psi_3}{\partial \xi} \right|_{\eta=0} = & \left[ -\frac{\partial \psi_1}{\partial \eta} \mathcal{Y}_2 - \frac{\partial^2 \psi_2}{\partial \xi \partial \eta} \mathcal{Y}_1 - \frac{\partial^2 \psi_1}{\partial \xi \partial \eta} \mathcal{Y}_2 - \frac{\partial^3 \psi_1}{\partial \xi \partial \eta^2} \mathcal{Y}_1^2 / 2 \right]_{\eta=0} \\ & + \cos \tau \sin \xi \chi_1^2 / 2 + \cos \tau \cos \xi \chi_2 + \sin \tau \cos \xi \chi_{2\tau} + \sin \tau \sin \xi \chi_1 \chi_{1\tau}. \end{aligned} \quad (4.17)$$

We put off further discussion of the second- and third-order terms in order to determine the minimal calculations needed to extract the leading term in the swimming speed,  $\langle \dot{\chi} \rangle$ . We shall show below that the first non-zero contribution is the third-order term  $\langle \dot{\chi}_3 \rangle$ . An understanding of the terms needed to obtain this contribution will determine the necessary higher-order calculations.

4.4. Calculation of the drift at third order

The drift at this order is given by

$$\langle \dot{\chi}_3 \rangle \equiv U_3 = \left\langle \left\langle \left[ \frac{\partial^3 \psi_1}{\partial \eta^3} \mathcal{Y}_1^2 / 2 + \frac{\partial^2 \psi_1}{\partial \eta^2} \mathcal{Y}_2 + \frac{\partial^2 \psi_2}{\partial \eta^2} \mathcal{Y}_1 + \frac{\partial \psi_3}{\partial \eta} \right]_{\eta=0} \right\rangle \right\rangle, \quad (4.18)$$

$$= U_3^{(1)} + U_3^{(2)} + U_3^{(3)} + U_3^{(4)}. \quad (4.19)$$

Two of these terms are easily calculated from the first-order results. We note first that

$$\begin{aligned} \left\langle \left\langle \left[ \frac{\partial^3 \psi_1}{\partial \eta^3} \right]_{\eta=0} \mathcal{Y}_1^2 / 2 \right\rangle \right\rangle &= \frac{1}{4} \left\langle \left[ \frac{\partial^3 \psi_{10}}{\partial \eta^3} \right]_{\eta=0} \sin^2 \tau \right\rangle \\ &= \frac{R}{4} \text{Re}(A) \equiv U_3^{(1)}. \end{aligned} \quad (4.20)$$

Also

$$\begin{aligned} \left\langle \left\langle \left[ \frac{\partial^2 \psi_1}{\partial \eta^2} \right]_{\eta=0} \mathcal{Y}_2 \right\rangle \right\rangle &= -\frac{1}{2} \left\langle \left[ \frac{\partial^2 \psi_{11}}{\partial \eta^2} \right]_{\eta=0} \chi_1 \sin \tau \right\rangle \\ &= \frac{1}{8} \text{Re}(iK^* A) \equiv U_3^{(2)}, \end{aligned} \quad (4.21)$$

where  $K^* = \sqrt{1 - iR}$ .

4.5. Contributions from the second-order terms

The remaining two terms require a partial knowledge of  $\psi_2$ . In particular

$$\left\langle \left\langle \left[ \frac{\partial^2 \psi_2}{\partial \eta^2} \right]_{\eta=0} \mathcal{Y}_1 \right\rangle \right\rangle = \frac{1}{2} \left\langle \left[ \frac{\partial^2 \psi_{21}}{\partial \eta^2} \right]_{\eta=0} \sin \tau \right\rangle \equiv U_3^{(3)}. \quad (4.22)$$

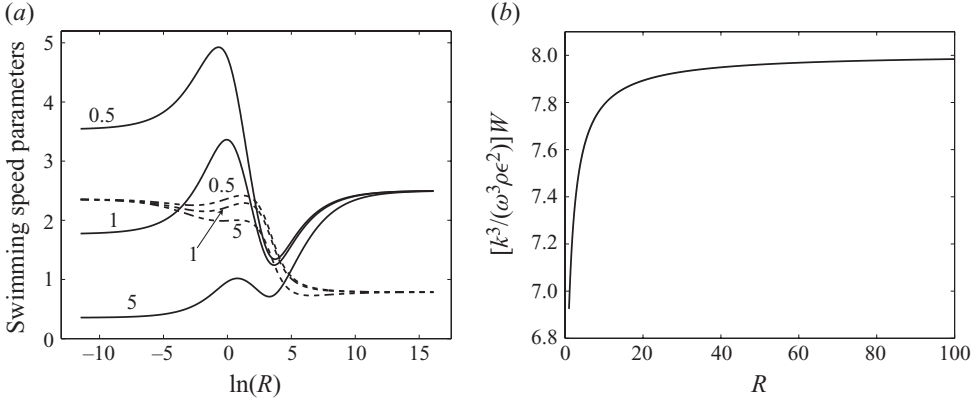


FIGURE 9. (a)  $10F(R, \beta)$  (solid line) and  $\Theta(R, \beta)$  (dashed line) as functions of  $\ln(R)$ , for the indicated values of  $\beta$  (see (4.27)). (b) The normalized work done by the upper surface of the raft, per unit length, as a function of  $R$  for  $\alpha = 1$ ,  $\beta = 1/2$  (see (4.34)).

Also

$$\left\langle \left\langle \left[ \frac{\partial \psi_3}{\partial \eta} \right]_{\eta=0} \right\rangle \right\rangle \equiv U_3^{(4)} \quad (4.23)$$

must be evaluated from the averages of (4.15):

$$-\frac{1}{R} \frac{\partial^4 \langle \psi_3 \rangle}{\partial \eta^4} = \frac{1}{2} \left\langle \frac{\partial \psi_{21}}{\partial \eta} \frac{\partial^2 \psi_{11}}{\partial \eta^2} + \psi_{21} \frac{\partial^3 \psi_{11}}{\partial \eta^3} - \frac{\partial \psi_{11}}{\partial \eta} \frac{\partial^2 \psi_{21}}{\partial \eta^2} - \psi_{11} \frac{\partial^3 \psi_{21}}{\partial \eta^3} \right\rangle. \quad (4.24)$$

Two integrations using the boundary condition on  $\psi$  at infinity yield

$$-\frac{1}{R} \frac{\partial^2 \langle \psi_3 \rangle}{\partial \eta^2} = \frac{1}{2} \left\langle \psi_{21} \frac{\partial \psi_{11}}{\partial \eta} - \psi_{11} \frac{\partial \psi_{21}}{\partial \eta} \right\rangle, \quad (4.25)$$

from which

$$U_3^{(4)} = \frac{R}{2} \int_0^\infty \left\langle \psi_{21} \frac{\partial \psi_{11}}{\partial \eta} - \psi_{11} \frac{\partial \psi_{21}}{\partial \eta} \right\rangle d\eta. \quad (4.26)$$

The calculations needed to complete the evaluation of  $U_3^{(3)}$ ,  $U_3^{(4)}$  are described in the Appendix. The results of this calculation are shown in figure 9(a). Here we set

$$U = \epsilon^3 U_3 = \alpha \epsilon^3 F(R, \beta) \sqrt{R} \cos(2\theta + \Theta(R, \beta)), \quad |\Theta| \leq \pi, \quad (4.27)$$

and plot  $10F(R, \beta)$  and  $\Theta(R, \beta)$  as functions of  $\ln(R)$  for several  $\beta$ .

It can be shown that  $F(R) \rightarrow 1/4$  and  $\Theta \rightarrow \pi/4$  as  $R \rightarrow \infty$ . Note that there are cancelling contributions of order  $R$ , as for example in  $U_3^{(1)}$ . The correct interpretation of this limit is discussed in the next section. As  $R \rightarrow 0$ , the calculations indicate that  $F$  has a positive limit, giving a swimming speed  $O(\epsilon^3 \sqrt{R})$ . This is appropriate to our infinite-sheet model but would presumably not be obtained for a finite body. Locomotion in that case should result from the shape-dependent drag in Stokes flow, which would give a speed of order  $R$  times a power of the amplitude of the shape change.

#### 4.6. Work

The work  $W$  done by the upper surface of the raft, per unit length, consists of two parts,  $W = W_s + W_m$ . The first part  $W_s$  is the average work done by the stress tensor

at the boundary:

$$W_s = -\langle\langle u(\sigma_{11}n_1 + \sigma_{12}n_2) + v(\sigma_{21}n_1 + \sigma_{22}n_2) \rangle\rangle_{y=y_B}, \tag{4.28}$$

where  $(n_1, n_2)$  is the outward unit vector normal to the boundary and

$$\sigma = \begin{pmatrix} -p + 2\mu \frac{\partial u}{\partial x} & \mu \left( \frac{\partial u}{\partial y} + \frac{\partial v}{\partial x} \right) \\ \mu \left( \frac{\partial u}{\partial y} + \frac{\partial v}{\partial x} \right) & -p + 2\mu \frac{\partial v}{\partial y} \end{pmatrix} \tag{4.29}$$

is the stress tensor. The second part  $W_m$  is the work per unit length done to move the masses:

$$W_m = \frac{mk}{\pi} \langle \dot{x}(\ddot{x} + \ddot{X}) \rangle = \frac{mk}{\pi} \langle \dot{x} \ddot{X} \rangle. \tag{4.30}$$

Passing to dimensionless variables, we find that the dominant contributions come from the products of the leading terms of our expansions in  $\epsilon$  at fixed  $R$  for  $\psi$  and  $\chi$ . Using the fact that  $\partial\psi_{11}(\xi, 0, \tau) = 0$  we find that

$$W_s = -\frac{\omega^3 \rho \epsilon^2}{k^3} \left\langle \frac{\partial^2 \psi_{10}}{\partial \eta^2} \dot{\chi}_1 + \frac{1}{2} \frac{\partial^3 \psi_{11}}{\partial \eta^3} \cos \tau \right\rangle_{\eta=0}. \tag{4.31}$$

Using (4.9) and (4.10) we obtain

$$W_s = \frac{\omega^3 \rho \epsilon^2}{k^3} \left( 4R^{-1/2} |A|^2 + \frac{1}{4} \text{Re}[K(K+1)R^{-1}] \right). \tag{4.32}$$

We also find

$$W_m = 4 \frac{\omega^3 \rho \epsilon^2}{k^3} \frac{\alpha}{\beta} \text{Im} \left[ \frac{i\alpha}{1 + \frac{\pi\beta(1-i)}{\sqrt{R}}} \right]. \tag{4.33}$$

Thus we can write

$$W = \frac{\omega^3 \rho \epsilon^2}{k^3} G(\alpha, \beta, R). \tag{4.34}$$

The function  $G(1, 1/2, R)$  is shown in figure 9(b). At the asymptote the work is entirely associated with moving the mass, and  $W = W_m = 4\alpha^2/\beta$  as  $R \rightarrow \infty$ . Note that (4.34) is independent of the phase angle  $\theta$ , as a result of the origin of the work from the leading orders of our expansions.

#### 4.7. The Stokes limit

We briefly consider the limit  $R \rightarrow 0$  of  $U_3(R)$  and justify the observed behaviour. We may disregard the nonlinear terms of the Navier–Stokes equations, which eliminates  $U_3^{(4)}$ . Also, clearly  $U_3^{(1)} \sim O(R^{3/2})$  as  $R \rightarrow 0$ . For  $U_3^{(3)}$  we have (the  $f_i$  below being coefficients in the eigenfunction expansion of  $\psi_{21}$ ; see the Appendix)

$$f_1 = \frac{3}{4} + O(R^{1/2}), \quad f_2 = -\frac{1}{2} + O(R^{1/2}), \quad f_3 = iR^{-1} + \frac{3}{2}i(1+i)R^{-1/2} - \frac{3}{2} + O(R^{1/2}), \tag{4.35}$$

$$f_4 = -iR^{-1} - \frac{3}{2}i(1+i)R^{-1/2} + \frac{3}{4} + O(R^{1/2}), \tag{4.36}$$

as  $R \rightarrow 0$ . Thus

$$M \sim A \left( \frac{3}{4} - \frac{1}{2} + f_3 + (1+iR)f_4 \right) \tag{4.37}$$

as  $R \rightarrow 0$  so that

$$U_3^{(3)} \sim \frac{1}{8} \operatorname{Re}(iA). \quad (4.38)$$

Together with  $U_3^{(2)}$  we therefore have

$$U_3 = \frac{\alpha}{8\beta} \operatorname{Re}[(1+i)e^{-2i\theta} R^{1/2} + O(R)] \sim \frac{\alpha}{4\sqrt{2}\beta} R^{1/2} \cos(2\theta + 3\pi/4). \quad (4.39)$$

We thus recover the behaviour shown for small  $R$  in figure 9(a).

We remark that the factor  $\sqrt{R}$  in the order  $\epsilon^3 \sqrt{R}$  of the swimming speed shows that the raft does not locomote in Stokes flow for  $R=0$ . The square root arises from the infinite geometry. The underlying oscillation of the raft comes from equating the reaction force exerted by the moving mass,  $4\omega^2 mL \sin 2(\tau - \theta)$ , with the drag computed as in §2.4 for the Rayleigh problem. This gives  $A \sim [(i-1)\alpha]/2\beta\sqrt{R}$ , in agreement with (3.24) for small  $R$ .

## 5. Large $R$ and the inviscid fluid

### 5.1. The large- $R$ limit as a singular perturbation

The calculations of the previous section are for fixed  $R$  and small  $\epsilon$ . The question of the analysis of Taylor's swimming sheet in the simultaneous limit of small  $\epsilon$  and large  $R$  was considered in Childress (2008), using the method of matched asymptotic expansions. At issue was the correct interpretation of the large- $R$  limit of the order  $\epsilon^2$  term in the expansion of the swimming speed at fixed  $R$ . The calculations were performed in two cases: a sinusoidal progressive wave of deformation of amplitude  $\epsilon$  and a sinusoidal wave of stretching of amplitude  $\epsilon$  of a horizontal sheet. Using expansions in both  $\epsilon$  and  $R^{-1/2}$ , Childress (2008) found that in the former case the appropriate expansion is for small  $\delta \equiv \epsilon \sqrt{R}$  and  $R^{-1/2}$ . In the latter case the expansion proceeds in the powers of  $\epsilon$  and  $R^{-1/2}$ , and the  $O(\epsilon^2)$ ,  $R = \infty$  result of Tuck (1968) is in this case acceptable. The difference can be understood by the need to avoid separation of the boundary layer for the progressive wave. The assumption of small  $\delta$  ensures that the wave amplitude remains small compared with the boundary-layer thickness:  $\epsilon \ll R^{-1/2}$ . For the wave of stretching, the unseparated horizontal boundary layer exists in the limit  $R \rightarrow \infty$ .

It turns out that the infinite-sheet model of the present paper is similar to Taylor's progressive wave of shape and that for large  $R$  the expansion of the swimming velocity must take the form

$$\langle \dot{\chi} \rangle \sim \sum_{m \geq 1, n \geq 1} \delta^m R^{-n/2} U_{mn}, \quad (5.1)$$

From the results of §3 we see that the leading term of (5.1) is  $U_{32} = (\alpha/4) \cos(2\theta + \pi/4)$ . We have carried out a boundary-layer analysis of the model and developed inner and outer expansions in  $\delta$ ,  $R^{-1/2}$ , to the extent needed to verify the vanishing of  $U_{mn}$  up to  $U_{32}$ . We omit these results, which follow the general scheme laid out in Childress (2008) and are useful primarily as a check for large  $R$  on the direct calculation of the preceding section.

## 6. Recoil locomotion reconsidered

We study the inviscid problem again, using the perturbation approach. From the well-known expression for linear momentum in potential flow we have the

dimensionless dynamical balance

$$\dot{\chi} + 2\epsilon\alpha \cos 2(\tau - \theta) - \frac{\beta}{\pi} \int_0^{2\pi} \phi \mathbf{n} \cdot \mathbf{i} \, d\xi = 0, \tag{6.1}$$

where  $(u, v) = (\phi_\xi, \phi_\eta)$ ,  $\phi = \epsilon\phi_1 + \epsilon^2\phi_2 + \dots$  and  $\mathbf{n}$  is the outward unit vector normal to the upper surface. Now we have

$$-\int_0^{2\pi} \phi \mathbf{n} \cdot \mathbf{i} \, d\xi = \int_0^{2\pi} [\epsilon^2\phi_1(\xi, 0, \tau)\mathcal{Y}'_1 + \epsilon^3(\phi_2(\xi, 0, \tau)\mathcal{Y}'_1 + \phi_1(\xi, 0, \tau)\mathcal{Y}'_2 + v_1(\xi, 0, \tau)\mathcal{Y}'_1\mathcal{Y}'_1)] \, d\xi. \tag{6.2}$$

We recall that

$$\mathcal{Y}_1 = \sin \tau \sin \xi, \quad \mathcal{Y}_2 = -\chi_1 \sin \tau \cos \xi \tag{6.3}$$

and compute  $\phi_i$  from expansion of the kinematic equation

$$v = \mathcal{Y}_\tau + u\mathcal{Y}_\xi, \quad y = \mathcal{Y}. \tag{6.4}$$

Thus

$$v_1|_{\eta=0} = \partial_\tau \mathcal{Y}_1 = \cos \tau \sin \xi, \quad \phi_1 = -\cos \tau \sin \xi e^{-\eta}. \tag{6.5}$$

Also

$$v_2 = [-(dv_1/d\eta)\mathcal{Y}_1 + \partial_\tau \mathcal{Y}_1 + u_1 \partial_\xi \mathcal{Y}_1]_{\eta=0}. \tag{6.6}$$

Thus

$$\phi_2 = \frac{1}{4} \sin 2\tau \cos 2\xi e^{-2\eta} + (\chi_1 \sin \tau)_\tau \cos \xi. \tag{6.7}$$

We may then evaluate the right-hand side of (6.2) to obtain

$$-\int_0^{2\pi} \phi \mathbf{n} \cdot \mathbf{i} \, d\xi = -\pi\epsilon^3 \chi_1 \sin 2\tau + \pi \frac{\partial}{\partial \tau} (\sin^2 \tau \chi_1) + o(\epsilon^3). \tag{6.8}$$

Thus the dynamical balance becomes

$$\dot{\chi} + 2\epsilon\alpha \cos 2(\tau - \theta) - \pi\epsilon^3 \chi_1(t) \sin 2\tau + \pi \frac{\partial}{\partial \tau} (\sin^2 \tau \chi_1) = 0. \tag{6.9}$$

Therefore,

$$\chi(t) = \epsilon \chi_1 + \epsilon^3 \chi_3 + o(\epsilon^3), \quad \dot{\chi}_1 = -2\alpha \cos 2(\tau - \theta) \tag{6.10}$$

and

$$\dot{\chi}_3 = -\frac{1}{2} \alpha \beta [\cos 2\theta(1 - \cos 4\tau) - \sin 2\theta \sin 4\tau] - \beta \frac{\partial}{\partial \tau} (\sin^2 \tau \chi_1). \tag{6.11}$$

$$= -\frac{1}{2} \alpha \beta [\cos 2\theta(1 - \cos 2\tau + \cos 4\tau) + \sin 2\theta(-\sin 2\tau + \sin 4\tau)]. \tag{6.12}$$

This derives again the average locomotion speed  $\langle \dot{\chi} \rangle$  given by (3.9). We remark that a similar calculation can be carried out using the stream function.

### 7. Comparison of the raft and the shape-changing finite body

We now transform the parameters of the infinite raft to make it conform to our numerical experiments with the shape-changing elliptical body. One section of the raft of length  $\pi/k$  may be regarded as one of a sequence of finite shape-changing

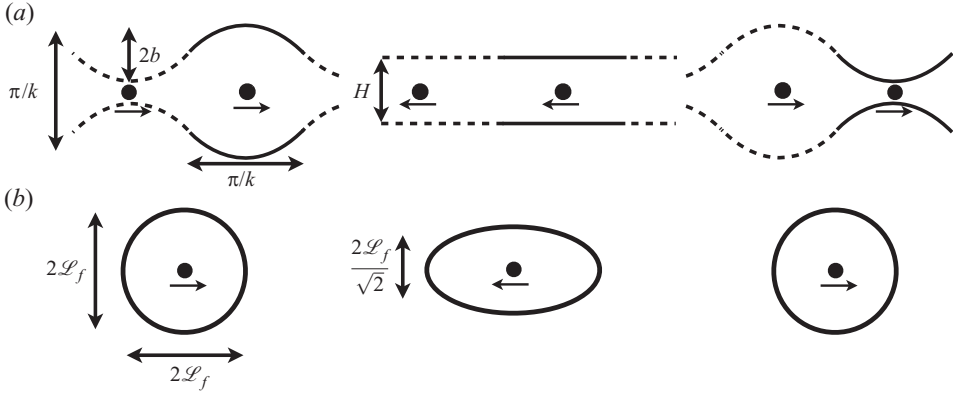


FIGURE 10. Comparison between (a) the infinite raft and (b) a finite shape-changing body. The upper and lower raft boundaries are taken to be separated by a distance  $H = 2\mathcal{L}_f/\sqrt{2}$ , and we choose  $2\mathcal{L}_f = \pi/k$  and  $H + 2b = \pi/k \implies b = \pi/(2k)(1 - 1/\sqrt{2})$ .

bodies. Because of the invariance of the infinite-raft boundary under simultaneous shifts of  $\tau$  and  $\xi$  by  $\pi/\omega$  and  $\pi/k$  respectively, we have

$$\omega_f = 2\omega. \quad (7.1)$$

(Recall that the subscript  $f$  corresponds to parameters associated with the finite body.) Figure 10 illustrates the parameter choices used in order to simulate the shape-changing finite body, using the infinite-sheet model. The upper and lower boundaries of the infinite raft may be separated by an arbitrary mean distance  $H$  without consequence on the fluid interactions considered in the earlier sections. In order to approximate the dynamics of the finite body, we choose  $\mathcal{L}_f = \pi/(2k)$ ,  $H = 2\mathcal{L}_f/\sqrt{2} = \pi/(\sqrt{2}k)$ , and (setting  $H + 2b = \pi/k$ ) we take the wave amplitude to be

$$b = (1 - 1/\sqrt{2})\mathcal{L}_f = \frac{\pi}{2k}(1 - 1/\sqrt{2}) \quad (7.2)$$

so that  $\epsilon = 0.46$ .

The relationship between Reynolds numbers is therefore

$$R_f = \rho \omega_f \mathcal{L}_f^2 / \mu = \frac{\pi^2 \rho \omega}{2k^2} / \mu = \frac{\pi^2 \rho \omega}{2k^2 \mu} = \frac{\pi^2}{2} R. \quad (7.3)$$

In addition, we have

$$\alpha_f = \frac{mL}{\mathcal{L}_f(M_0 + m)} = \frac{(1 - 1/\sqrt{2})mL}{b(M_0 + m)} = \left(1 - \frac{1}{\sqrt{2}}\right) \alpha \quad (7.4)$$

and

$$\beta_f = \frac{\pi \rho \mathcal{L}_f^2}{M_0 + m} = \frac{\pi^3 \rho}{4k^2(M_0 + m)} = \frac{\pi^2}{4} \beta. \quad (7.5)$$

Finally, if  $U_s$  is the dimensional swimming speed, then the dimensionless swimming speeds  $U_f$  and  $U$  are related via

$$U_f = \frac{U_s}{\mathcal{L}_f \omega_f} = \frac{k U_s}{\pi \omega} = \frac{1}{\pi} U. \quad (7.6)$$

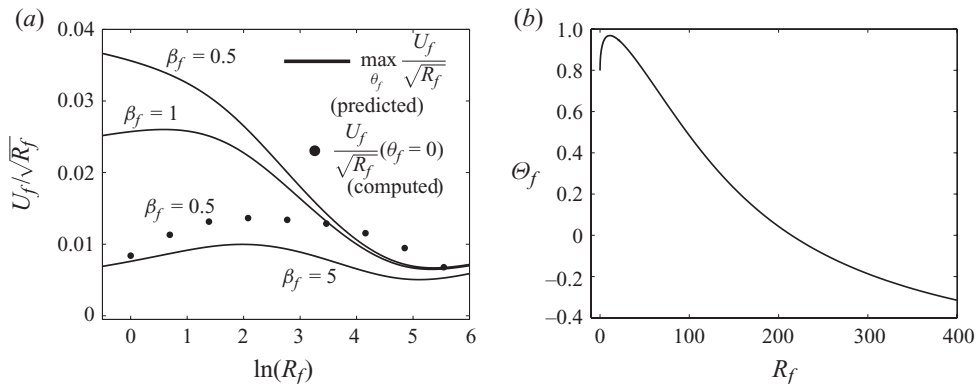


FIGURE 11. (a) Modelling a finite shape-changing body by the results for the infinite raft;  $\max_{\theta_f}(U_f/\sqrt{R_f})$  as a function of  $R_f$  for several values of  $\beta_f$  with  $\alpha_f = 1$ . (b) Comparison of the phase shift  $\Theta_f$  as a function of Reynolds number, for  $\alpha_f = 1$  and  $\beta_f = 1/2$ .

Using these parameters, the infinite-raft analysis predicts through (4.27) a dimensionless swimming velocity in the finite-body case of

$$\begin{aligned} \max_{\theta_f} \frac{U_f}{\sqrt{R_f}} &= \max_{\theta} \frac{\sqrt{2} U}{\pi^2 \sqrt{R}} = \frac{\sqrt{2}}{\pi^2} \alpha \epsilon^3 F(R, \beta) \\ &= \frac{\sqrt{2} \pi}{8} \left(1 - \frac{1}{\sqrt{2}}\right)^2 \alpha_f F(2R_f/\pi^2, 4\beta_f/\pi^2) \end{aligned} \quad (7.7)$$

(recall that  $\epsilon = kb$ ). Figure 11(a) shows the predicted values of  $\max_{\theta_f}(U_f/\sqrt{R_f})$  as a function of  $R_f$  for  $\alpha_f = 1$  and several values of  $\beta_f$ . The computed values of  $U_f/\sqrt{R_f}$  with  $\theta_f = 0$  are also included for comparison (from the inset of figure 5a). Given the difference of geometries and the probable interactions of neighbouring bodies, the discrepancy is not unexpected. For instance, the finite elliptic body undergoes area-preserving motions, while each half-wavelength of the infinite raft does not, though both are subject to the same recoil forcing. From this we expect the raft to locomote with a larger velocity at low Reynolds numbers (where the viscous drag is more important), which is what we observe. For larger Reynolds numbers, the pressure drag is dominant, and both models (from figure 10) are chosen to present the same extremal surface areas to the fluid; this may explain why the infinite-raft model better approximates the finite-body model as the Reynolds number increases.

Now consider a comparison of the phase shifts  $\Theta$  and  $\Theta_f$ . At  $\tau = 0$  we see from (2.20) and the  $\sin(\omega t)$  variation of  $Y(x, t)$  that with  $\omega$  halved the raft achieves maximal vertical deformation at  $\tau = \pi/2$ , while the finite body has its maximum at  $\tau = 0$ . Thus the only difference between the two models comes from the origin of the cycle of deformation chosen in each case. We should therefore have

$$\Theta_f = \Theta - \pi/2. \quad (7.8)$$

We show the predicted phase shift from the infinite-raft calculation (as in figure 9a, shifted by  $\pi/2$ ) as  $\Theta_f$  versus  $R_f$  in figure 11(b) for  $\alpha_f = 1$  and  $\beta_f = 1/2$ . This prediction is not close to the numerical results found for the finite body, as shown in figure 6(b).

We can discuss this discrepancy, using simple models. Consider first the finite body. We will try to model the system in the intermediate-Reynolds-number range by simply taking the viscous drag of the body to vary linearly with the vertical deformation.

Thus we take the position  $\chi(\tau)$  of the centre of volume to satisfy

$$\frac{d}{d\tau}(1 + \beta_f + a_f \epsilon^2 \cos \tau) \frac{d\chi}{d\tau} + f(R)(1 + b_f \epsilon^2 \cos \tau) \frac{d\chi}{d\tau} = \epsilon \alpha_f \sin(\tau - \theta_f). \quad (7.9)$$

We have introduced the small-amplitude  $\epsilon$  to allow an  $O(\epsilon)$  underlying oscillation  $\chi_0(\tau)$  which satisfies the equation if the terms involving the positive constants  $a_f, b_f$  are neglected:

$$\chi_0(\tau) = -\frac{\epsilon \alpha_f}{1 + \beta_f} \left( \frac{1}{1 + F^2} \sin(\tau - \theta_f) + \frac{F}{1 + F^2} \cos(\tau - \theta_f) \right), \quad (7.10)$$

where  $F = f/(1 + \beta_f)$ , and therefore, with  $\theta_f = 0$ ,

$$\frac{d\chi_0}{d\tau} = -\frac{\epsilon \alpha_f}{1 + \beta_f} \frac{1}{\sqrt{1 + F^2}} \cos(\tau + \tilde{\phi}_f), \quad \tilde{\phi}_f = \tan^{-1} F. \quad (7.11)$$

Comparing this last expression with (2.19), we see that  $f = C/\sqrt{R_f}$ .

To compute the resulting locomotion, we return to the full (7.9), to obtain upon averaging the approximate result

$$\begin{aligned} U_f = \langle \chi_\tau \rangle &\sim \frac{\epsilon^3 b_f \alpha_f}{1 + \beta_f} \frac{1}{\sqrt{1 + F^2}} \langle \cos \tau \cos(\tau - \theta_f + \tilde{\phi}_f) \rangle \\ &= \frac{1}{2} \frac{1}{\sqrt{1 + F^2}} \frac{\epsilon^3 b_f \alpha_f}{1 + \beta_f} \cos(\theta - \tilde{\phi}_f), \end{aligned} \quad (7.12)$$

from which we have  $\Theta_f = -\tilde{\phi}_f$ . This yields  $\Theta_f = -\pi/2$  for small  $R$  and  $\Theta_f \sim 0$  for large  $R$ . The small- $R_f$  behaviour is what is observed in figure 6(b). For large  $R_f$ ,  $\Theta_f$  rises above zero, a discrepancy which is not captured by our simple model.

For the infinite raft, on the other hand, the underlying oscillation has a velocity  $\epsilon d\chi_1/d\tau = \epsilon \operatorname{Re}(2iAe^{2i\tau})$ , where  $A$  is given by (3.24). To construct a simple model for the drift we assume that it is a response to differential drag associated with the bumps on the raft, which can be taken as proportional to the raft velocity times  $1 + \epsilon^2 \sin^2 \tau = -(1/2)\epsilon^2 \cos(2\tau) + \text{constant}$ . Thus

$$\langle \chi_\tau \rangle \sim -\frac{1}{2} C \epsilon^3 \langle \cos(2\tau) \operatorname{Re}(2iA e^{2i\tau}) \rangle = \frac{1}{2} C \epsilon^3 \operatorname{Re} \left[ \frac{\alpha e^{-2i\theta}}{1 + \frac{\beta(1-i)}{\sqrt{R}}} \right], \quad (7.13)$$

where  $C$  is the constant of proportionality. For small  $R$  we get

$$\langle \chi_\tau \rangle \sim \frac{b\epsilon^3 \alpha \sqrt{R}}{2\sqrt{2}\beta} \cos(2\theta + 3\pi/4), \quad (7.14)$$

which agrees with our asymptotic result (4.39) if  $C = 1/2$ . On the other hand as  $R \rightarrow \infty$ , it is seen from (7.14) that  $\Theta$  rotates counterclockwise to  $\pi$ , and  $|\langle \chi_\tau \rangle|$  increases modestly to a finite asymptote. Thus the model does not at all capture the intermediate- and large- $R$  behaviour. This is not surprising, since the large- $R$  limit for the raft is simultaneous with the limit of small  $\epsilon$ . It is likely to be difficult to capture with a simple model the nonlinear drag differentials experienced by small wall deformation within a thicker Rayleigh boundary layer. We also emphasize that for large  $R$  the finite body should be viewed as at fixed  $\epsilon$ , representing a distinctly different limit. Indeed the rough compatibility of the raft and finite-body calculations is restricted to very moderate Reynolds numbers.

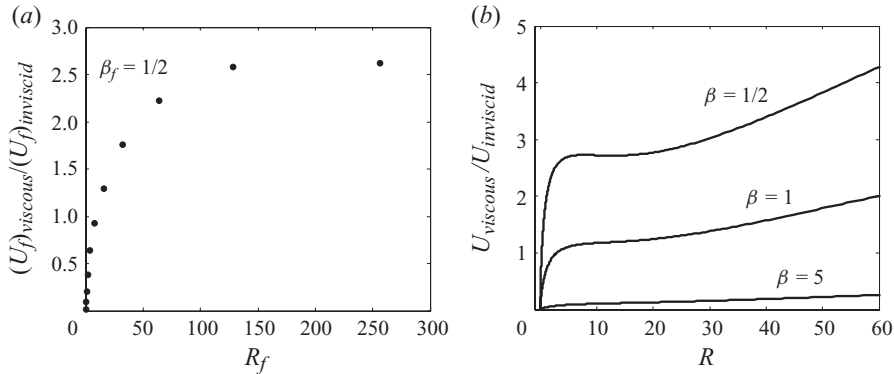


FIGURE 12. (a) Ratio of swimming speeds in the viscous and inviscid cases for the finite body (from figure 5a), with  $\theta_f = 0$ ,  $\alpha_f = 1$  and  $\beta_f = 1/2$ . (b) Ratio of maximum swimming speeds in the viscous (4.27) and inviscid (3.9) cases for the infinite raft, with  $\beta = 1/2, 1, 5$ .

To make the above comparisons we have applied a small- $\epsilon$  theory outside of its expected region of validity. The flow about the finite body involves well-defined vortex shedding in a region close to the body. While we have not made a study of the flow field of the infinite raft, the nonlinear interactions leading to the  $O(\epsilon^3)$  swimming speed should also involve moderate shedding of vorticity, and we feel what agreement there is in the predicted and measured values  $U_f(R_f)$  indicates that the role of this vortex shedding on both virtual mass and drag is not dissimilar in the two problems.

## 8. Discussion

Recoil locomotion was introduced in Saffman (1967) as a mechanism for swimming of a finite body in a perfect fluid. Locomotion arises from the simultaneous variation of the centre of mass of the body and its shape. The momentum associated with shape change is usually (but not necessarily) accompanied by variation of the virtual mass of the body. In the examples studied in the present paper, the centre of mass was altered by an internal moving mass, and the shape change was explicitly chosen to vary the virtual mass.

The purpose of the present paper has been to explore the mechanism of recoil swimming in a viscous fluid, over a range of Reynolds numbers including the so-called intermediate range  $R = 50\text{--}300$  as well as larger values  $R \sim 1000$ . A numerical exploration of recoil movements of a finite body of elliptical shape has been carried out. These calculations have been complemented by an analysis of a sheet model undergoing small oscillations of shape.

The principal new result of our investigation is the observed enhancement in both models of the maximum swimming velocity in a viscous fluid. For the finite body we found approximately 2–3 times the inviscid value in the examples studied, as shown in figure 12(a). Although we must there base our conclusions on a small-amplitude theory, the results for the infinite raft are consistent. We show in figure 12(b) the ratio of maximum viscous to maximum inviscid swimming speeds as a function of the Reynolds number for the raft. Note that to obtain the maximum the phase  $\theta$  must equal  $-\Theta(R)$  modulo  $\pi$  in the viscous case.

The effect of viscosity, interpreted as the introduction of dissipation, might be expected to reduce recoil locomotion, if not eliminate the mechanism entirely, and indeed this reduction is observed here at small Reynolds numbers. But at intermediate

Reynolds numbers, our observations show that the field of shed vorticity interacts with the body to augment the recoil force driving the underlying oscillation and thereby increases the swimming velocity. This raises the question of how one might maximize recoil swimming in a viscous fluid by departing from the mechanisms suggested by the inviscid case. Swimming in an irrotational fluid should be viewed as a quite distinct case.

We have studied recoil locomotion in a regime such that the motion ceases as the Reynolds number decreases to zero. However some recoil swimming is still possible in the Stokes limit if the recoil forcing scales appropriately with the Reynolds number. As long as the recoil force is large enough to move the body in an inertia-less system, the drag anisotropy at  $R=0$  is sufficient to yield locomotion. Many of the familiar means of locomotion in nature, through flagellar undulations, for example, or from flapping of wings, are of course effective only in certain Reynolds number regimes (see e.g. Childress 1981). Recoil locomotion, in contrast, is not so limited and can be an effective means of moving a body at all Reynolds numbers.

Another aspect deserving mention is the limited extent of the wake which is produced in some instances. Of course recoil locomotion can be achieved with no vorticity at all and typically with the decay of velocity at infinity of a potential dipole, although mechanisms for reducing this to a quadrupole may exist (Lighthill 1991). This far-field decay is sufficiently fast so that the so-called Stokes paradox in two dimensions does not play a role, and our results should extend to three-dimensional considerations without dramatic variation. In the viscous case at intermediate  $R$  the oscillatory nature of the ‘ratcheting’ mechanism keeps the boundary layer relatively close to the body. It would be interesting to explore the decay of fluid disturbances for these locomotors, to see to what degree one can achieve what we might call ‘stealth swimming’.

We are not aware of any obvious use in natural locomotion of the mechanisms studied in this paper. To be sure, Newton’s laws apply to all organisms, and recoil plays some role in all locomotion at sufficiently large Reynolds numbers. Changes of the centre of mass can be a natural accompaniment of changes of shape, and it is possible that recoil locomotion in nature exists in systems quite different from those studied in this paper. We have suggested in Childress (2010) that water-walking insects, which propel themselves by abrupt movements of their feet across the air–water interface (Bush & Hu 2006), might be viewed as using recoil locomotion. The viscous effects are evidenced there by the generation of vortex dipoles beneath the water surface. Kanso *et al.* (2005) have studied a three-link swimmer in an inviscid fluid which utilizes variations in the centre of mass in conjunction with variations in virtual mass, a motion which may involve elements of the recoil locomotion. The same swimmer in a viscous fluid was studied by Eldredge (2006), who showed that in this undulatory swimming motion, viscous dissipation acts to reduce the swimming speed even at higher Reynolds numbers. Shape-changing locomotion of jellyfish may also be related to the present considerations (see Daniel 1983, 1984). The expulsion of fluid and the formation of a vortex wake do not seem to have any counterpart in the present models, however. Finally, a recent study by Simon *et al.* (2010) has shown that the gut of a crawling caterpillar slides forward in advance of surrounding tissues so that the animal’s centre of mass is decoupled from visible translations of the body. Perhaps, then, such internal-mass oscillations are also exploited by swimming organisms of a related evolutionary path, though this remains to be seen.

In the light of these results we may thus summarize ‘the peculiar role of viscosity’, alluded to in the Introduction, as follows. At low Reynolds numbers, recoil swimming

is greatly diminished unless a large mass redistribution is available. At intermediate Reynolds numbers, recoil swimming is significantly enhanced. And the limit of large Reynolds number is quite distinct from the inviscid theory.

The research reported in this paper was supported by the National Science Foundation under grant no. 0507615 at New York University.

Supplementary movies of recoil swimming by the finite body are available at [journals.cambridge.org/flm](http://journals.cambridge.org/flm).

**Appendix. The calculation of  $U_3^{(3)}$  and  $U_3^{(4)}$**

We indicate, omitting some details, the calculation of the final two contributions to  $U_3$ , which involve the second-order terms in  $\psi$ . The first task is to calculate the needed parts of  $\psi_{21}$ . This term has components proportional to  $\sin \tau$ ,  $\cos \tau$ ,  $\sin 3\tau$  and  $\cos 3\tau$ , but only the former two are needed in (4.22) and (4.26) (see (4.9)–(4.11)). We thus set

$$\psi_{21} = \text{Re}[\psi_{211} e^{i\tau} + \psi_{213} e^{3i\tau}], \quad \psi_{10} = \text{Re}[\psi_{102} e^{2i\tau}], \quad \psi_{11} = \text{Re}[\psi_{111} e^{i\tau}] \quad (\text{A } 1)$$

and consider now only  $\psi_{211}$ . The equation for this term is seen to be

$$\partial_\tau(\partial_\eta^2 - 1)\psi_{211} - \frac{1}{R}(\partial_\eta^2 - 1)^2\psi_{211} = \frac{1}{2}[\partial_\eta\psi_{102}(\partial_\eta^2 - 1)\psi_{111}^* - \psi_{111}^*\partial_\eta^3\psi_{102}] \equiv F_{211}. \quad (\text{A } 2)$$

Using (4.9) and (4.10) we have

$$F_{211} = A \left[ \exp[(\sqrt{2iR} + K^*)\eta] \left( -i(1 + K^*) + \frac{2R}{1 - K^*} \right) + \frac{2RK^*}{K^* - 1} \exp[-(1 + \sqrt{2iR})\eta] \right]. \quad (\text{A } 3)$$

Integrating, and using the boundary conditions at infinity, we obtain

$$\psi_{211} = A[f_1 \exp[(\sqrt{2iR} + K^*)\eta] + f_2 \exp[-(1 + \sqrt{2iR})\eta] + f_3 \exp(-\eta) + f_4 \exp(-K\eta)], \quad (\text{A } 4)$$

where

$$f_1 = \frac{3R}{(K^* - 1)[8(i + R) + 2i\sqrt{2iRK^*}]}, \quad f_2 = \frac{2RK^*}{(K^* - 1)(2R - 8i - 6i\sqrt{2iR})}. \quad (\text{A } 5)$$

The multipliers  $f_3$ ,  $f_4$  are determined by the boundary conditions on  $\psi_{211}$  at  $\eta = 0$ . These are obtained from

$$\partial_\xi\psi_2|_{\eta=0} = \partial_\tau(\chi_1 \sin \tau) \cos \xi, \quad \chi_1 = \text{Re}(A e^{2i\tau}), \quad (\text{A } 6)$$

$$\partial_\eta\psi_2|_{\eta=0} = -\mathcal{D}_{10}\partial_\eta^2\psi_1|_{\eta=0}. \quad (\text{A } 7)$$

From these there results

$$\psi_{211}|_{\eta=0} = -A/2, \quad \partial_\eta\psi_{211}|_{\eta=0} = (1 + i)A\sqrt{R}. \quad (\text{A } 8)$$

With the  $f_i$  now determined, we have from (4.22)

$$U_3^{(3)} = \frac{1}{4}\text{Re}(iM), \quad (\text{A } 9)$$

where

$$M = A[f_1(\sqrt{2iR} + K^*)^2 + f_2(1 + \sqrt{2iR})^2 + f_3 + K^2 f_4]. \quad (\text{A } 10)$$

Turning finally to  $U_3^{(4)}$ , we have from (4.26)

$$-\frac{1}{R}\partial_\eta^2\langle\langle\psi_3\rangle\rangle = \frac{1}{4}\text{Re}[\psi_{211}\partial_\eta\psi_{111}^* - \psi_{111}^*\partial_\eta\psi_{211}]. \quad (\text{A } 11)$$

Thus

$$U_3^{(4)} = \frac{R}{4}\int_0^\infty \text{Re}[\psi_{211}\partial_\eta\psi_{111}^* - \psi_{111}^*\partial_\eta\psi_{211}] d\eta. \quad (\text{A } 12)$$

The integral may be evaluated explicitly, since the integrand is a sum of exponentials.

#### REFERENCES

- ALBEN, S. 2008 An implicit method for coupled flow-body dynamics. *J. Comput. Phys.* **227**, 4912–4933.
- BRAZA, M., CHASSAING, P. & HA MINH, H. 1986 Numerical study and physical analysis of the pressure and velocity fields in the near wake of a circular cylinder. *J. Fluid Mech.* **165**, 79–130.
- BUSH, J. W. M. & HU, D. L. 2006 Walking on water: biolocomotion at the interface. *Annu. Rev. Fluid Mech.* **38**, 339–369.
- CHILDRESS, S. 1981 *Mechanics of Swimming and Flying*. Cambridge.
- CHILDRESS, S. 2008 Inertial swimming as a singular perturbation. In *Proceedings of the ASME 2008 Dynamic Systems and Control Conference, Ann Arbor, MI*. Available at: <http://www.math.nyu.edu/faculty/childres/preprints.html>.
- CHILDRESS, S. 2010 Walking on water. *J. Fluid Mech.* **644**, 1–4.
- DANIEL, T. L. 1983 Mechanics and energetics of medusan jet propulsion. *Can. J. Zool.* **61**, 1406–1420.
- DANIEL, T. L. 1984 Unsteady aspects of aquatic locomotion. *Amer. Zool.* **24**, 121–134.
- E, W. & LIU, J. G. 1996 Essentially compact schemes for unsteady viscous incompressible flows. *J. Comput. Phys.* **126**, 122–138.
- ELDRIDGE, J. D. 2006 Numerical simulations of undulatory swimming at moderate Reynolds number. *Bioinsp. Biomim.* **1**, S19–S24.
- ELSTON, J. R., BLACKBURN, H. M. & SHERIDAN, J. 2006 The primary and secondary instabilities of flow generated by an oscillating circular cylinder. *J. Fluid Mech.* **550**, 359–389.
- KANSO, E., MARSDEN, J. E., ROWLEY, C. W. & MELLI-HUBER, J. 2005 Locomotion of articulated bodies in a perfect fluid. *J. Nonlinear Sci.* **15**, 255–289.
- LIGHTHILL, J. 1991 Hydrodynamic far fields. In *Mathematical Approaches in Hydrodynamics* (ed. T. Miloh), pp. 3–20. Society of Industrial and Applied Mathematics.
- ROSHKO, A. 1961 Experiments on the flow past a circular cylinder at very high Reynolds number. *J. Fluid Mech.* **10**, 345–356.
- SAFFMAN, P. G. 1967 Self-propulsion of a deformable body in a perfect fluid. *J. Fluid Mech.* **28**, 385–389.
- SIMON, M. A., WOODS, W. A. JR, SEREBRENİK, Y. V., SIMON, S. M., VAN GRIETHUIJSEN, L. I., SOCHA, J. J., LEE, W-K. & TRIMMER, B. A. 2010 Visceral-locomotory pistoning in crawling caterpillars. *Curr. Biol.* **20**, 1–6.
- SPAGNOLIE, S. E. & SHELLEY, M. J. 2009 Shape-changing bodies in fluid: hovering, ratcheting, and bursting. *Phys. Fluids* **21**, 013103.
- TATSUNO, M. & BEARMAN, P. W. 1990 A visual study of the flow around an oscillating circular cylinder at low Keulegan–Carpenter numbers and low Stokes numbers. *J. Fluid Mech.* **211**, 157–182.
- TAYLOR, G. I. 1951 Analysis of the swimming of microscopic organisms. *Proc. R. Soc. Lond. A* **209**, 447–461.
- TUCK, E. O. 1968 A note on the swimming problem. *J. Fluid Mech.* **31**, 305–308.